Interannual Teleconnections in the Sahara Temperatures Associated with the North Atlantic Oscillation (NAO) during Boreal Winter

Liming Zhou[1], Wenjian Hua[2], Sharon E. Nicholson[3], Joseph P. Clark[4]

[1]*Department of Atmospheric and Environmental Sciences, University at Albany, State University of New York (SUNY), Albany, NY 12222, USA*

[2]*School of Atmospheric Sciences, Nanjing University of Information Science and Technology, Nanjing 210044, China*

[3]*Department of Earth, Ocean and Atmospheric Science, Florida State University Tallahassee, FL 32306, USA*

[4]*Program in Atmospheric and Oceanic Sciences, Princeton University, Princeton, NJ 08540, USA*

Correspondence

Liming Zhou

Department of Atmospheric and Environmental Sciences

University at Albany, State University of New York

1400 Washington Avenue, Albany, NY 12222

Tel: (518) 442-4446; Fax: (518) 442-5825

ORCID: https://orcid.org/0000-0002-7009-2487

https://www.atmos.albany.edu/facstaff/zhou/lzhou.html

Email: lzhou@albany.edu

Zhou, L., Hua, W., Nicholson, S.E. *et al.* Interannual teleconnections in the Sahara temperatures associated with the North Atlantic Oscillation (NAO) during boreal winter. *Clim Dyn* **62**, 1123–1143 (2024). https://doi.org/10.1007/s00382-023-06962-w.

Received 25 May 2023; Accepted 10 September 2023; Published 28 September 2023; Issue Date February 2024.

Abstract. The North Atlantic Oscillation (NAO) is the most recognized and leading mode of atmospheric variability observed over the Atlantic sector of the Northern Hemisphere, and its impacts on weather and climate over the North Atlantic and Eurasia via large-scale teleconnections have been extensively studied. Here we use a multidata synthesis approach to analyze surface and tropospheric variables from multiple long-term observational and reanalysis datasets to identify the NAO's footprint on interannual temperature variability over the vast but least-studied Sahara Desert during December–January–February–March for the satellite era (1979-2022) and century-long periods. Our results present evidence for a solid teleconnection pattern in surface and tropospheric temperatures associated with the NAO over the Sahara and document some major spatial–temporal and vertical characteristics of this pattern. It is found that the Saharan temperature anomalies are negatively correlated with the NAO index and this correlation is very strong, consistent, and statistically significant between different periods and across different datasets. The teleconnection is closely linked to large-scale circulation anomalies throughout the troposphere over the North Atlantic–Sahara sector, where the anomalous horizontal wind components and geopotential height exhibit opposite changes in sign with altitude from the lower to upper troposphere. During the negative NAO− (positive NAO+) phase, above-normal (below-normal) temperatures over the Sahara could be mainly explained by three major processes: (1) advection of climatological warm and moist (cold and dry) air over the North Atlantic (northern higher latitudes) by the anomalous southwesterly (northeasterly) flow in the lower troposphere; (2) advection of anomalous North Atlantic warm (cold) air by the climatological strong westerlies in the middle and upper troposphere; and (3) strengthened (weakened) vertical mixing in the atmospheric boundary layer. These results suggest that the NAO plays an important role in modulating the interannual temperature variability over the Sahara, and that this NAO footprint is mostly realized through horizontal temperature advection and vertical heat transfer by turbulent mixing.

Key words: North Atlantic Oscillation (NAO), teleconnection, Sahara Desert, interannual temperature variability

1. Introduction

The harsh and hyper-arid Sahara Desert (shortly referred to as the Sahara hereafter) in northern Africa is the largest hot desert on Earth due to the combination of regional continental geography and large-scale atmospheric circulation patterns (Wu et al., 2009; Zhang et al., 2014; Pausata et al., 2020). Paleoclimate proxies indicate that the Sahara has undergone major hydrological fluctuations between wet conditions with lush trees, grasses, and permanent lakes, and dry conditions with limited vegetation in the deep past (Castañeda et al., 2009; Menviel et al., 2021). On geological time scales, these fluctuations are believed to have been initially triggered by changes in radiative forcing due to gradual variations in Earth's orbital parameters and atmospheric concentrations in greenhouse gases (GHGs) and sustained and enhanced by a host of remote and local nonlinear feedback processes involving changes in local vegetation and remote sea surface temperatures (SSTs) (Wright, 2016; Pausata et al., 2020).

On interannual and decadal time scales, recent studies of instrumental records, reanalysis data, and climate model simulations have documented amplified surface warming over the vast Sahara and Arabian deserts in recent decades (Collins, 2011; Cook and Vizy, 2015; Zhou et al., 2015; 2016; 2021; Zhou, 2016; 2021; Vizy and Cook, 2017; Evan et al., 2017; Wei et al., 2017). This large-scale warming pattern, termed "desert amplification", is attributed possibly to a stronger greenhouse effect over drier ecoregions in response to a warmer and moister atmosphere with increasing GHGs. Interestingly, these studies also show strong interannual variability in temperatures over the Sahara and Arabian deserts. With suppressed convection and extreme dry and mostly cloudless weather conditions, the subtropical deserts have relatively stable surface conditions in terms of surface albedo, vegetation, and soil moisture. On interannual time scales, small variations in solar insolation and anthropogenic GHGs cannot explain substantial year-to-year temperature variations over the deserts. Possibly, remote forcing, such as changes in SSTs and large-scale circulations, could be the dominant contributors to the Saharan interannual temperature variability.

One such contributor is the North Atlantic Oscillation (NAO), which has long been recognized as the dominant mode of winter atmospheric variability in the Northern Hemisphere (NH) (van Loon

and Rogers, 1978; Rogers and van Loon, 1979; Barnston and Livezey, 1987; Wallace and Gutzler, 1981). The NAO is often defined by the NAO index (NAOI), which describes changes in the strength of two recurring sea level pressure (SLP) patterns over the North Atlantic involving the polar Icelandic Low and the subtropical Azores High (e.g., Hurrell, 1995; 1996; Visbeck et al., 2001). Positive NAOI values (i.e., positive NAO phases) correspond to above-normal SLP and geopotential height (GPH) over the central North Atlantic and western Europe, and below-normal SLP and GPH across the high-latitude North Atlantic. In contrast, negative NAOI values (i.e., negative NAO phases) exhibit the opposite patterns over these regions. Both positive and negative NAO phases are associated with basin-wide changes in the intensity and location of jet streams and storm tracks, and in large-scale modulations of the normal patterns of zonal and meridional heat and moisture transport (Hurrell, 1995; 1996). These changes and modulations result in considerable anomalies in temperature, moisture, and precipitation on a wide range of time scales from days to centuries in Europe, Greenland, North America, and northern Asia (e.g., Hurrell, 1995; 1996; Visbeck et al., 2001; Hurrell and Deser, 2009; Moulin et al., 2017; Ma and Zhang, 2018; Nie et al., 2020).

Fluctuating atmospheric and oceanic conditions associated with the NAO in the North Atlantic region have strong impacts on surrounding regions and weather and climate in downstream and remote regions across the NH (Visbeck et al., 2001; Li and Ruan, 2018). The NAO exerts dominant impacts on wintertime temperatures across much of the NH, and its variability is significantly correlated with surface air temperature and SSTs across wide regions of the North Atlantic Ocean, North America, the Arctic, Eurasia, and the Mediterranean (Hurrell, 1995; 1996; Hurrell et al., 2003; Pinto and Raible, 2012). Considering its proximity to the North Atlantic Ocean and direct exposure to the North Atlantic atmospheric circulation, the Sahara is likely to be subject to the influences of the NAO.

Among many published papers related to the NAO, only several have examined the NAO's impacts over Africa. In terms of precipitation, Meehl and van Loon (1979) first demonstrated an association between the NAO and the position of the intertropical convergence zone during December–February over Africa; Lamb and Peppler (1987) noted a significant inverse relationship in the interannual variations between the NAOI and Moroccan boreal winter precipitation, driven

by the southward displacement of the North Atlantic storm track and precipitation-bearing storms when the North Atlantic westerlies are weak; and McHugh and Rogers (2001) described negative and highly significant correlations between the NAOI and December–February rainfall variability over southeastern Africa (0°–16°S and 25°–40°E), due to anomalous moisture and circulation fields associated with the positive/negative NAO phases. In terms of temperature, Hurrell et al. (2003) briefly mentioned the cooling of North Africa and the Middle East when the NAOI is positive in explaining their Fig. 13; Nigam and Baxter (2015) showed in their Fig. 4 that the strongest impacts of the NAO on surface temperature emerge over Europe and northern Africa, and the positive NAO results in above-normal temperatures over nearly all of Europe, while below-normal temperatures prevail from Saharan Africa east-northeastward to the eastern Mediterranean, Middle East, and the Arabian Peninsula; and Clark and Feldstein (2020a) illustrated in their Fig. 1 the composite surface temperature anomaly patterns for the positive and negative NAO phases in the NH including North Africa from the ERA-Interim reanalysis. However, the focus of these three papers is on the NH and particularly, only one sentence is mentioned when referring to one plot showing the Saharan temperature anomalies associated with the NAO phases in each paper.

Although the structure of the prominent teleconnection patterns such as the NAO has been known for several decades, the physical mechanisms that govern the NAO and its variability and how the NAO responds to external forcing are not yet well understood and still under debate (e.g., Visbeck et al., 2001; Nigam, 2003; Hurrell et al., 2003). To date, the NAO's impacts on weather and climate anomalies have been often attributed to NAO-induced large-scale circulation anomalies and associated zonal and meridional heat and moisture transport (Hurrell, 1995; 1996; Hurrell et al., 2003; Nigam and Baxter, 2015). The physical mechanisms in explaining the NAO impacts on surface air temperature (SAT) are summarized in Clark and Feldstein (2020a). According to Clark and Feldstein (2020a), past studies have concluded that SAT anomaly patterns for both positive and negative NAO phases are mainly driven by horizontal temperature advection (e.g., van Loon and Rogers, 1978; Rogers and van Loon, 1979; Wallace and Gutzler, 1981; Watanabe, 2004; Woollings et al., 2008; Hurrell et al., 2003; Nigam and Baxter, 2015). This viewpoint is consistent with maps of anomalous SLP, from which the implied direction of the anomalous winds relative to the climatological temperature gradient suggests the observed SAT anomaly pattern. In addition,

the spatial pattern of horizontal temperature advection associated with the NAO resembles the NAO's SAT anomaly pattern, further confirming this viewpoint (e.g., Clark and Feldstein, 2020b).

To attribute the NAO impacts on both surface and atmospheric temperature anomalies, Clark and Feldstein (2020a; 2020b) conducted a comprehensive composite analysis of the thermodynamic energy equation over the NH using ERA-Interim reanalysis. They found that the advection of the climatological temperature field by the anomalous wind makes the largest contribution to the NAO-driven temperature anomaly patterns throughout the troposphere, while the advection of anomalous temperature by the climatological wind is the most important contributor to temperature changes in the upper troposphere. In addition, they included a detailed analysis of all major heating processes over four selected regions, including northern Africa where the diabatic heating term of vertical mixing mainly opposes the horizontal temperature advection in the boundary layer, while latent heating plays a minor role. Clark and Feldstein (2020b) also showed that anomalous adiabatic warming/cooling largely opposes NAO-related temperature anomaly growth over the Sahara (their Fig. 3), a finding they note to be consistent with the quasigeostrophic omega equation. In other words, when the NAO is active, suppressed (enhanced) subsidence coincides with warm (cold) air advection over the Sahara.

Despite its importance to Earth's weather and climate, the Sahara has a significant data gap which fundamentally inhibits our understanding of the Saharan meteorology because of inadequate observations available for data collection, assimilation, or model validation (Washington et al., 2013; Zhou, 2021). Consequently, our understanding of the Saharan climate and our modeling capacities are very limited with large uncertainties, and there is a critical need to overcome this limitation and fill in our knowledge gap using more independent datasets and methods over the data-scarce Sahara. The recent availability of several observational and reanalysis datasets with improved quality and longer periods provides a great opportunity to validate and further understand the NAO impacts on Saharan temperature variability.

As the center of the subtropical Azores High spans the central North Atlantic and much of North Africa, we expect to see the NAO footprint in key weather variables such as SLP and surface temperature over the Sahara. The aforementioned studies, however, have not completely addressed

how the NAO impacts the Saharan interannual temperature variability. Furthermore, previous studies of NAO impacts have mostly focused on temperature and precipitation in the northern middle and high latitudes; among the few studies related to Africa the emphasis has been on rainfall. In order to elaborate on the NAO's impacts on temperature over northern Africa as touched upon previously by several studies, here we present the very first comprehensive and detailed regional study of the NAO teleconnection patterns over the vast Sahara.

The motivation for this study is threefold. The first goal is to use a multidata synthesis approach from an ensemble of different observational and reanalysis datasets with improved quality to corroborate previous findings of the NAO's impacts on surface temperatures. By considering both the sign and statistical significance of the NAO-induced anomalies, we look for the NAO signal that is robust and consistent to increase our confidence in the obtained results. The second goal is to investigate the robustness and persistence of the NAO's impact on Sahara temperatures and assess the uncertainty using different datasets with much longer records. In particular, we will compare the results from the satellite era to those from several century-long observational datasets and account for errors in the forecast model and uncertainties in observations and differences in construction methods using two century-long ensemble reanalyses. The third goal is to examine both surface and tropospheric variables to understand the vertical structure of tropospheric air temperature changes associated with the NAO over the Sahara. Previous studies have focused mostly on surface temperatures, but temperature changes are not limited to the Earth surface and can be extended into the free atmosphere (Zhou, 2021). The vertical structure of temperature changes can tell a whole story of the NAO's impacts. Our primary focus is to document the NAO teleconnection patterns over the vast Sahara and establish their spatiotemporal and vertical features on interannual time scales, while the possible physical mechanisms are developed mostly by synthesizing our results with previous research.

2. Data and Methods

2.1. Study region and periods

The emphasis of this study is on: (1) the Sahara Desert, but hemispheric analyses are also performed to identify the large-scale features of NAO teleconnections, which can be validated with previous findings; (2) the four winter months, December–January–February–March (DJFM), when the NAO signal is strongest (e.g., Hurrell, 1995; 1996; Hurrell et al., 2003; Visbeck et al., 2001; Pinto and Raible, 2012). The study is focused on two periods. The first one covers the modern satellite era from 1979 to 2022, to maximize the data coverage of various measurements used in observational and reanalysis products over the data-scarce desert regions (Zhou, 2021). The second period extends the satellite-era study back as early as 1864 to maximize the temporal coverage of in-situ measurements to a much longer time scale. As the NAO's impacts are not limited only to the surface, the atmospheric variables in the troposphere will also be analyzed.

2.2. Observational and reanalysis datasets

We examine two widely used and independently derived monthly NAOI datasets from observations. The first one is station-based using the difference of normalized SLP between Lisbon, Portugal, and Stykkisholmur/Reykjavik, Iceland, for the period 1864-2022, provided by the National Center for Atmospheric Research (NCAR) (https://climatedataguide.ucar.edu/climate-data/). The second one is obtained by projecting the NAO loading pattern onto monthly mean 500 hPa GPH anomalies for the period 1950-2022 over the NH based on a Rotated Empirical Orthogonal Function analysis and standardized by the 1950–2000 base period monthly means and standard deviations (Barnston and Livezey, 1987; van den Dool et al., 2000; Chen and van den Dool, 2003), provided by the National Oceanic and Atmospheric Administration (NOAA) (https://www.ncdc.noaa.gov/teleconnections/nao/). These two standardized NAOI datasets are hereafter referred to as the NCAR and NOAA NAOI, respectively.

The latest versions of two well-documented global gridded monthly mean surface temperature datasets are analyzed. The first one is NASA's Goddard Institute for Space Studies (GISS) Surface Temperature Analysis version 4 (GISTEMP v4) on a 2º latitude by 2º longitude grid for the period 1880-2022 (https://data.giss.nasa.gov/gistemp/). It is produced by combining satellite observations, SST records from the Extended Reconstructed Sea Surface Temperature version 5

(ERSSTv5) dataset, and meteorological station measurements from the NOAA's Global Historical Climatology Network (GHCNv4) (GISTEMP Team, 2021; Lenssen et al., 2019). The second dataset is the Berkeley Earth Surface Temperatures (BEST) on a 1º latitude by 1º longitude grid for the period 1850-2022 (https://berkeleyearth.org/data/). It is created by combining the Berkeley Earth monthly land temperature field with the spatially kriged version of the Met Office Hadley Centre's SST dataset (HadSST3) (Rohde and Hausfather, 2020). The BEST is intended to provide an alternative, independent assessment of global surface temperature, separate from the analyses of NOAA and NASA. Note that both datasets are developed by combining 2 m surface air temperature over land with SSTs over ocean. These two observational surface temperature datasets are hereafter referred to as the GISS and Berkeley temperatures, respectively.

The Global Historical Climatology Network Monthly Version 4 (GHCNMv4) contains monthly mean temperatures for over 26,000 stations across the globe for the period 1880-2022 (https://www.ncei.noaa.gov/pub/data/ghcn/v4/). The GHCNMv4 is the NOAA's latest station-based dataset that uses the same quality control and bias correction algorithms as version 3 but has included a greatly expanded set of stations (Menne et al., 2018). It is updated periodically using comprehensive data collections of increased global area coverage over both land and ocean surfaces to provide the most accurate depiction of environmental conditions and has been frequently used in global gridded datasets, and NOAA's monthly climate reports as well as other national and international climate assessments. This study uses 2m air temperatures of 53 weather stations over the Sahara from the GHCNMv4 and the regional averaged monthly temperature anomalies from these stations are calculated to study the long-term Saharan temperature variability (1880-2022). Note that this regional mean temperature anomaly time series may be subject to inhomogeneities because these weather stations are concentrated in limited areas and differ in temporal coverage (e.g., Cook and Vizy, 2015; Zhou, 2021). As stated previously, it has been challenging to study climate change in data-sparse regions such as the Sahara due to the lack of high-density and temporally consistent long-term in situ measurements. Nevertheless, this dataset, together with the others introduced in this section, are used here as sources of information about surface temperature variability over the Sahara. This station-based dataset is hereafter referred to as the GHCNMv4 temperatures.

We use the 5th generation European Centre for Medium-Range Weather Forecasts (ECMWF) Reanalysis (ERA5; Hersbach et al., 2020), a state-of-the-art global atmospheric reanalysis dataset spanning the period 1979–2022. The ERA5 is produced by combining vast amounts of historical observations into global estimates using advanced modeling and data assimilation systems (C3S, 2017). The ERA5 monthly mean meteorological fields analyzed consist of (1) three-dimensional data on pressure levels: temperature (ºC), specific humidity (g kg^{-1}), horizontal wind (u and v, m s^{-1}), vertical velocity (ω, Pa s^{-1}), and GPH (m); and (2) two-dimensional data on single levels: mean SLP (hPa), 2 m air temperature (°C), 2 m specific humidity (g kg^{-1}), 10 m horizontal wind (m s^{-1}), and SST (ºC), on a 1° longitude × 1° latitude grid. To be consistent with the GISS and Berkeley temperatures, the corresponding ERA5 surface temperatures are developed by combining the ERA5 2 m air temperatures over land with SSTs over oceans. The ERA5 offers data on 37 pressure levels and here we only consider the following 12 mandatory pressure levels: 1000, 925, 850, 700, 600, 500, 400, 300, 250, 200, 150, and 100 hPa. Note that 100 hPa is below the tropopause over the Sahara and so all these levels are confined to the troposphere. For subsequent reference, we broadly divide the troposphere into three layers (e.g., Lau and Kim, 2015): the lower troposphere (below 700 hPa), the middle troposphere (from 700 hPa to 400 hPa), and the upper troposphere (above 400 hPa).

We also considered utilizing the second Modern-Era Retrospective Analysis for Research and Applications (MERRA-2) for the period 1980-2022, a NASA atmospheric reanalysis making enhanced use of satellite observations (Gelaro et al., 2017). However, the results are very similar to those in the ERA5 and thus are not included here to avoid redundancy.

In addition, this study analyzes two widely-used century-long climate reanalyses to examine the robustness and persistence of the teleconnection patterns identified from the modern-era reanalyses: (1) the NOAA–CIRES–DOE Twentieth Century Reanalysis version 3 (20CRv3) provided by the NOAA/Physics Science Laboratory (PSL) (Slivinski et al., 2019); (2) the Coupled Reanalysis for the 20th Century (CERA-20C) provided by the ECMWF (Laloyaux et al., 2018). The 20CRv3 is produced by assimilating only surface pressure observations and prescribing sea surface temperature, sea ice concentration, and radiative forcings into NOAA's Global Forecast System to estimate the most likely state of the global atmosphere from 1806 to 2015. It contains

objectively analyzed 4-dimensional weather maps and their uncertainty from a set of 80-member ensemble analyses. The 20CRv3 dataset consists of the ensemble mean and standard deviation (or ensemble spread) for each variable on a 1° longitude × 1° latitude grid (http://apdrc.soest.hawaii.edu/datadoc/20century_reanalysisV3.php). The CERA-20C is produced by ECMWF's coupled ocean–atmosphere assimilation system that assimilates only surface pressure, ocean surface winds, and ocean temperature and salinity measurements with the fifth phase of the Coupled Model Intercomparison Project (CMIP5) atmospheric forcing to reconstruct the past weather and climate of the Earth system covering the period 1901–2010. The CERA-20C reanalysis and its 10 ensemble members at a horizontal resolution of 1° are available at https://www.ecmwf.int/en/forecasts/datasets/reanalysis-datasets/cera-20c. The two reanalyses with multiple ensemble members can provide an assessment of both model and observation uncertainty. It is worth noting that these two century-long reanalyses rely on a consistent (but restricted) set of long-term observations and do not assimilate upper-air (i.e., radiosonde) and modern-era satellite observations (post-1979) to avoid possible spurious artificial trends due to changes in the underlying observational network (Thorne and Vose, 2010). Therefore, they differ substantially and independently from modern-era reanalyses (e.g., ERA5 and MERRA-2) constrained by a full suite of observational datasets (Wohland et al., 2020; Agrawal et al., 2021). Here monthly mean 2m surface air temperatures from both reanalyses are examined as the reanalyses are constrained by surface observations and the NAO has the strongest impact on surface variables (section 3).

2.3. Data processing and methods

Among the above five global gridded datasets (i.e., Berkeley, GISS, ERA5, 20CRv3, and CERA-20C), GISS has a coarser spatial resolution and so is re-projected onto the common 1° by 1° grid boxes of the other four datasets using bilinear interpolation. For a given variable, the monthly mean anomaly from January to December in each year is first calculated by subtracting its monthly climatology from the monthly mean; the monthly mean anomalies are then averaged for the four winter months December–January–February–March (DJFM)), i.e., December of previous year and January to March of current year, to obtain the yearly DJFM mean anomaly time series for the study periods.

This study is concerned with interannual temperature variability and so the long-term warming trend during the study periods should be excluded. The least squares linear trend is estimated and removed from the satellite-era time series of DJFM anomalies whose warming trends are close to a straight line. A high-pass filter could be used to remove the decadal variability (e.g., for a frequency longer than 7 years) for the century-long time series of data, but this filtering has a very limited impact on the results presented and so is not considered.

To identify the teleconnection patterns associated with the NAO, we primarily use correlation analysis to quantify the relationship between two variables (e.g., Wallace and Gutzler, 1981; Lamb and Peppler, 1987; McHugh and Rogers, 2001; Pinto and Raible, 2012; Nigam and Baxter, 2015; Li and Ruan, 2018). For example, the NAOI can be correlated with the GPH and wind anomalies to establish the NAO teleconnection patterns with large-scale circulation anomalies. A Student's-*t* test is used to assess the statistical significance (p value) of the correlation coefficient (R).

Composite analysis is often used to identify the teleconnection patterns associated with positive and negative NAO phases (e.g., Wallace and Gutzler, 1981; Hurrell 1995; 1996; Visbeck et al., 2001; Pinto and Raible, 2012; Martineau et al., 2020). Figure 1a shows interannual variations in the standardized DJFM NAOI for the period 1979–2022 from the NCAR and NOAA datasets, indicating strong year-to-year variations between positive and negative NAO phases and a record-breaking negative NAOI in 2010 (e.g., Osborn, 2011) during the 44-year period. Here we define the representative positive NAO (i.e., NAO+) and negative NAO (i.e., NAO−) phases as the years with the standardized NAOI > +1 STD and < −1 STD, respectively, from both the NCAR and NOAA datasets. There are six NAO+ years: 1983, 1989, 1995, 2012, 2015, and 2020, and six NAO− years: 1979, 1996, 2001, 2010, 2011, and 2013, chosen for composite analysis. Evidently, the two NAOI datasets are highly correlated ($R=0.92$, $p < 0.001$) and so their average standardized NAOI is hereafter used to represent the observed NAOI during the satellite era.

The statistical significance of the composite anomalies is estimated based on Monte Carlo simulation (Qin et al., 2020). For a given time series of 44 years of data (e.g., temperature) from 1979 to 2022, the difference between the composite mean from the 6 years of NAO+ (NAO−)

phases and the mean of any randomly chosen 6 years is tested for statistical significance, as follows, First, we randomly choose 6 years from the 44 years of anomaly data and calculate the 6-year mean of anomalies. We repeat this process 1000 times and obtain an empirical distribution of the 1000 6-year means. Second, we calculate the actual composite mean from the 6 years of NAO+ (or NAO−) phases, respectively. If the actual composite mean exceeds the 95th percentile or is less than the 5th percentile of the empirical distribution, the composite anomalies from NAO+ and NAO- phases are considered statistically significant at the 10% level ($p<0.10$). Here the level of statistical significance is chosen as 10% for the composite analysis, rather than 5% for the correlation analysis, due to the small sample size of our composite.

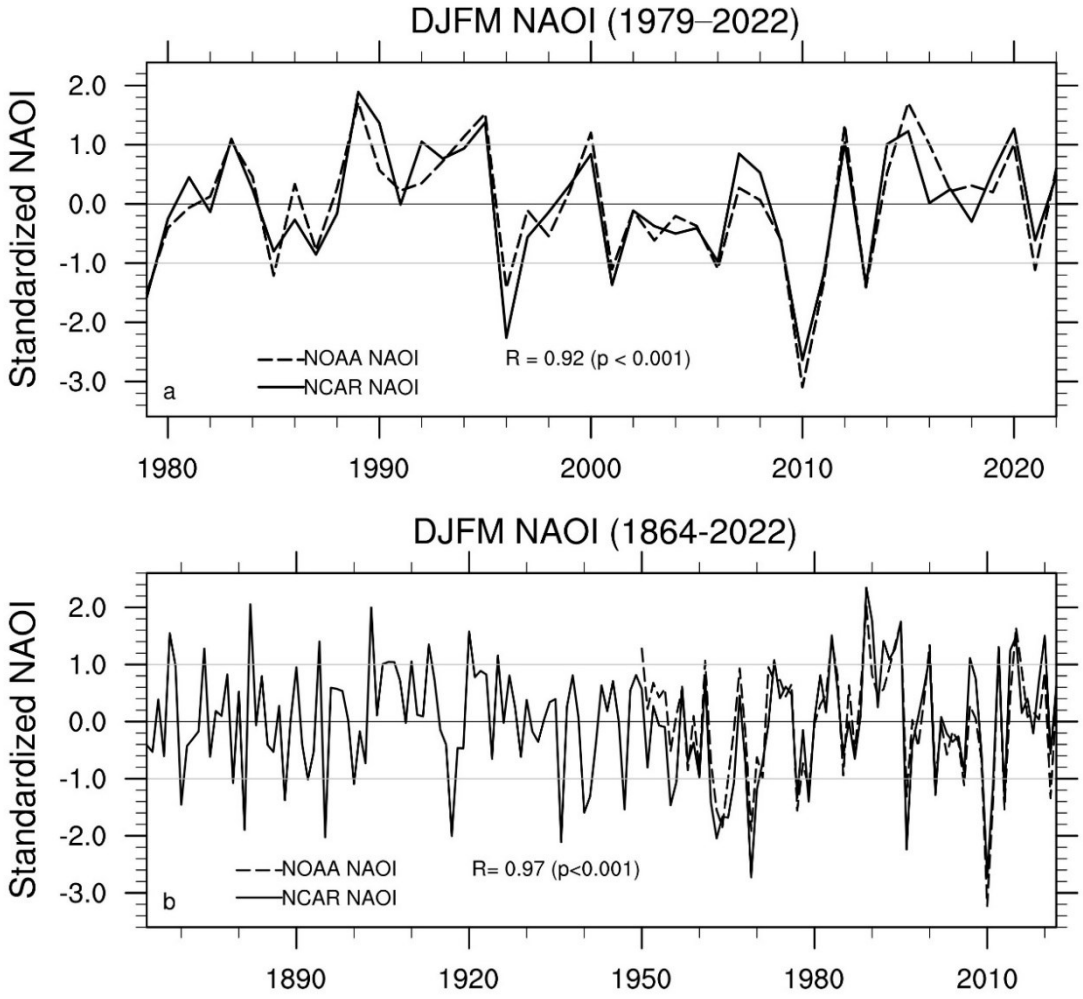

Fig. 1. *Interannual variations in standardized NAOI during DJFM for the period (a) 1979–2022 and (b) 1864-2022 from the NCAR and NOAA datasets. The one standard deviation (±1 STD) lines (in gray) are drawn for reference. The correlation coefficient (R) and its significance level (p value) between the two indices are shown.*

Regional mean quantities for the Sahara are calculated using area-weighted averaging over the inner domain of the desert, which corresponds to the green rectangle (20°N–30°N, 15°W–35°E) depicted in Fig. 3c, following previous studies (e.g., Cook and Vizy, 2015; Vizy and Cook, 2017; Evan et al., 2017). The regional mean temperature anomaly time series is termed the Saharan temperature index (STI).

It is reasonable to believe that the modern-era reanalyses are of high quality in describing the past atmospheric conditions by combining vast amounts of historical observations into global estimates using advanced modelling and data assimilation systems. Hence, our regionally focused analyses of atmospheric variables over the Sahara are only done with the ERA5. Note that the NAO footprint on the Saharan temperatures is most evident in the troposphere and so our discussion is concerned with this layer of the atmosphere. In addition, every variable analyzed in this study is a 4-monthly mean quantity during DJFM, and for brevity, the term ‘‘DJFM’’ is often omitted for the remainder of this paper.

3. Results and discussion

3.1. Large-scale teleconnection patterns during the satellite era

In this subsection we analyze the large-scale teleconnection patterns on hemispheric scales for the period 1979–2022 to gain some background knowledge before focusing on our regional study domain. It is essential that ERA5 can capture the major observed features in interannual temperature variability before being used for further diagnostic analysis. Note that the standardized averaged NAOI from the two NAOI datasets is used to represent the observed NAOI (Fig. 2) here.

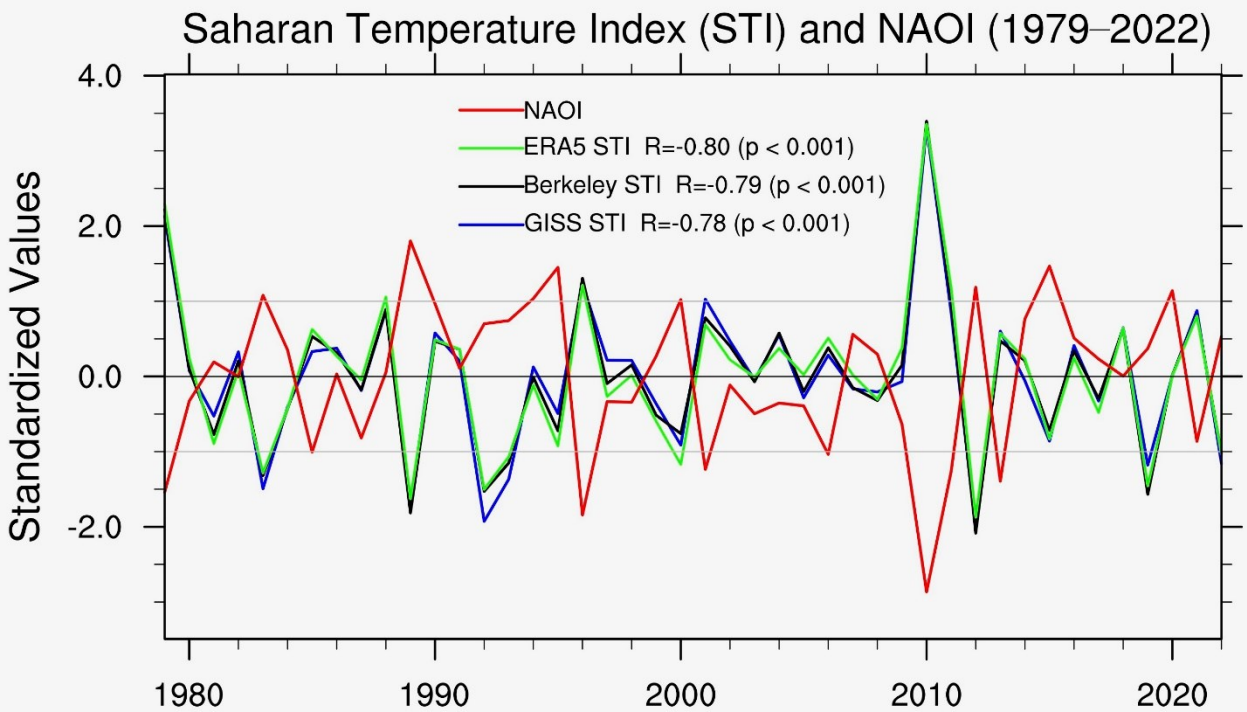

Fig. 2. *Interannual variations in standardized NAOI (Fig. 1) and Saharan temperature index (STI) for the period 1979–2022 from the GISS, Berkeley, and ERA5. The STI is calculated as the regional mean temperature anomalies averaged over the inner domain of the Sahara Desert (20°N–30°N, 15°W–35°E, depicted in Fig. 3c). The one standard deviation (±1 STD) lines (in gray) are drawn for reference. The correlation (R) and its significance level (p value) between the NAOI and temperature anomalies are shown. The NAOI is the average standardized NAOI from the NCAR and NOAA NAOI (Fig. 1a).*

Figure 2 displays interannual variations in STI and NAOI for the period 1979-2022. Despite strong interannual variations, the NAOI is significantly correlated negatively with the temperatures from GISS ($R=-0.78$, $p < 0.001$), Berkeley ($R=-0.79$, $p < 0.001$), and ERA5 ($R=-0.80$, $p < 0.001$), indicating above-normal (below-normal) temperature anomalies during the NAO− (NAO+) phases. Clearly, the three surface temperature datasets show almost identical variability, so that the average STI from the two observational datasets (Berkeley and GISS) is hereafter used to represent the observed STI during the satellite era unless otherwise specified.

Figures 3a-c show the spatial pattern of correlation (R) between NAOI and gridded surface temperatures in the NH from the GISS (Fig. 3a), Berkeley (Fig. 3b), and ERA5 (Fig. 3c) datasets. Evidently, all three datasets exhibit similar large-scale spatial features across the NH, characterized predominantly by bipolar teleconnection patterns over land (e.g., Stephenson et al., 2003).

Statistically significant positive correlations are seen over much of the U.S., Europe, and northern Asia, while statistically significant negative correlations are observed over northern Canada, Greenland, northern Africa, the Middle East, and southwestern Asia. Regionally, the NAO footprint on SSTs reveals a characteristic tripolar pattern over the North Atlantic Ocean, with negative correlations in the subpolar region, positive correlations in the subtropics, and again negative correlations in the tropics. The large-scale coherence in negative correlations over northern Africa and the Middle East is compelling. In contrast, the correlations of the NAOI with the Southern Hemispheric temperatures are very weak and statistically insignificant (not shown for brevity), consistent with previous findings that the NAO is primarily confined to the NH (e.g., Visbeck et al., 2001; Hurrell et al., 2003; Pinto and Raible, 2012; Nigam and Baxter, 2015).

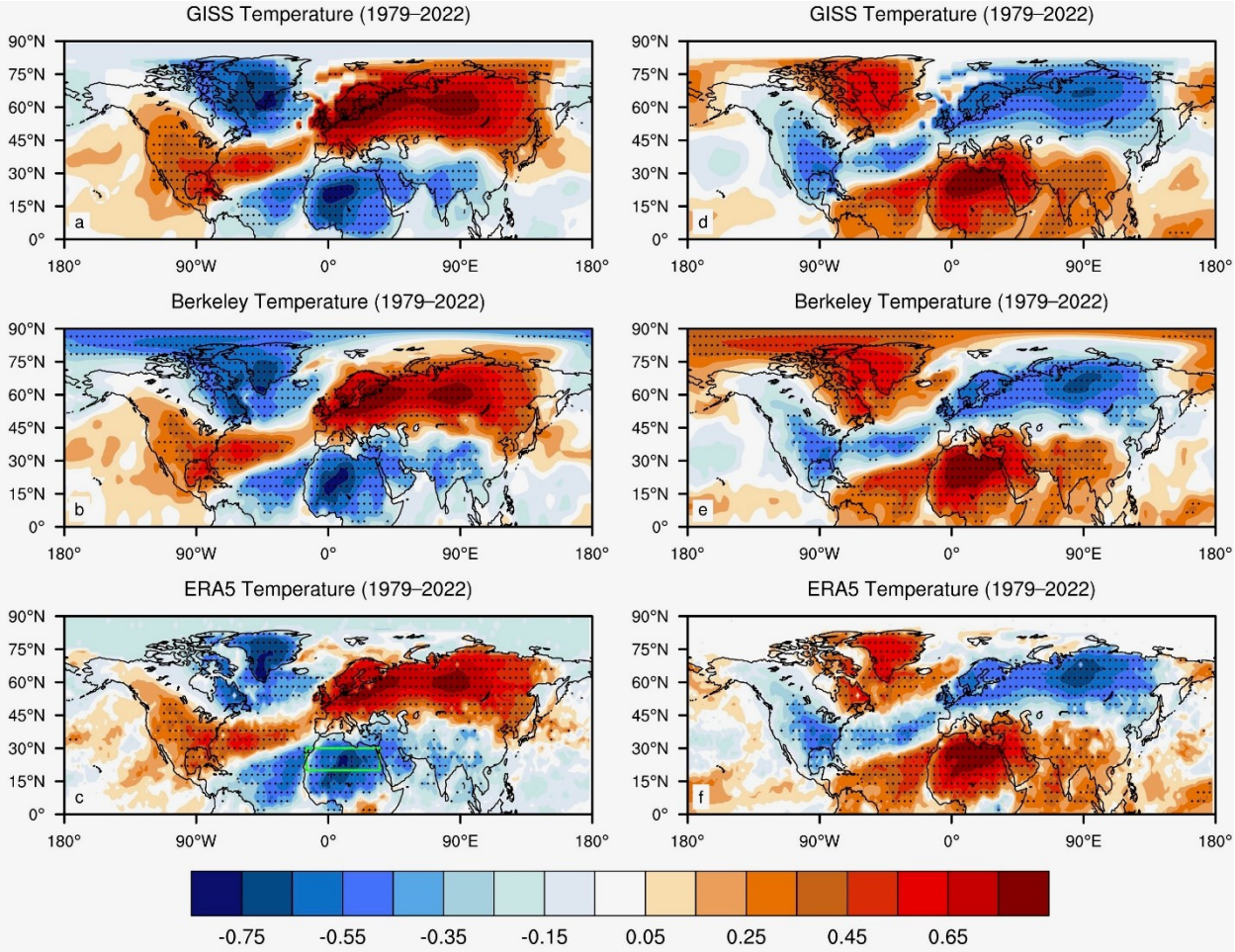

Fig. 3. *Spatial patterns of correlation between NAOI (Fig. 2) and surface temperature in the Northern Hemisphere (NH) for the period 1979–2022 from the three temperature datasets: (a) GISS, (b) Berkeley, and (c) ERA5. Stippling indicates that the correlation coefficient is statistically*

significant at the 5% level ($p < 0.05$). The green rectangle (20°N–30°N, 15°W–35°E) depicted in Fig. 3c represents the inner domain of the Sahara Desert where regional mean quantities are calculated. The surface temperatures in the three datasets are created by combining 2 m surface air temperature over land with SSTs over ocean. (d)-(f) are the same as (a)-(c) except for the correlation with the observed STI, which is the average STI from the two observational datasets (Berkeley and GISS) (Fig. 2).

One alternative way to test whether the NAO is the dominant factor in controlling the Saharan interannual temperatures is to do a similar correlation analysis as in Figs. 3a-c but replacing the NAOI by the STI. The spatial patterns of this correlation (Figs. 3d-f) are almost identical to those in Figs. 3a-c except with opposite signs, which is expected given the strong negative correlation between the NAOI and STI (Fig. 2). The nearly perfect spatial correspondence with opposite correlations over almost every grid between Figs. 3a-c and Figs. 3d-f highlights the dominant role of the NAO in influencing the Saharan interannual temperatures.

Figures 4a-d show the spatial patterns of correlations of the NAOI with SLP and GPH at three tropospheric levels in the NH between 90ºW–90ºE from the ERA5. Strong and significant negative correlations in SLP and 850 hPa GPH with the NAOI are seen throughout the Arctic, while strong and significant positive correlations are observed across the subtropical and tropical Atlantic. The largest correlation centers are associated with the Icelandic Low and the Azores High. The NAO signal is consistent with its historical characterization as a north–south dipole in SLP that represents out-of-phase fluctuations of the Icelandic Low and Azores High. These dipolar patterns in SLP/GPH are predominantly equivalent barotropic with a high degree of vertical coherence over the North Atlantic–European sector (e.g., Pinto and Raible, 2012; Nigam and Baxter, 2015). Over the North Atlantic–Sahara sector, positive correlations cover almost the entire Sahara at the surface and in the lower troposphere, but these positive correlations transition into negative correlations in the middle and upper troposphere over much of the Sahara.

Figures 4e-h are the same as Figs. 4a-d except for the correlations with the STI. As expected, the correlation patterns resemble those in Figs. 4a-d except with opposite signs given the strong negative correlation between the NAOI and STI (Fig. 2).

The results in this subsection reaffirm previous studies on the hemispheric-scale teleconnection patterns between the NAO and surface temperature in the NH (e.g., Hurrell et al., 2003; Nigam and Baxter, 2015; Clark and Feldstein, 2020a) and reveal that the ERA5 surface temperature has reproduced the observed teleconnection patterns from the Berkley and GISS temperatures (Figs. 2-3). At regional scales, two major features stand out over our study domain. One is the strong and significant negative NAOI–STI correlations (Fig. 2), indicating warmer (colder) surface temperatures than climatology over the Sahara during the NAO− (NAO+). The other is the large-scale coherent and zonally oriented patterns of statistically significant correlations that extend eastward from the tropical and subtropical North Atlantic to the Sahara (Figs. 3-4), suggesting a strong link between the Saharan temperatures and the North Atlantic SSTs via the NAO teleconnections.

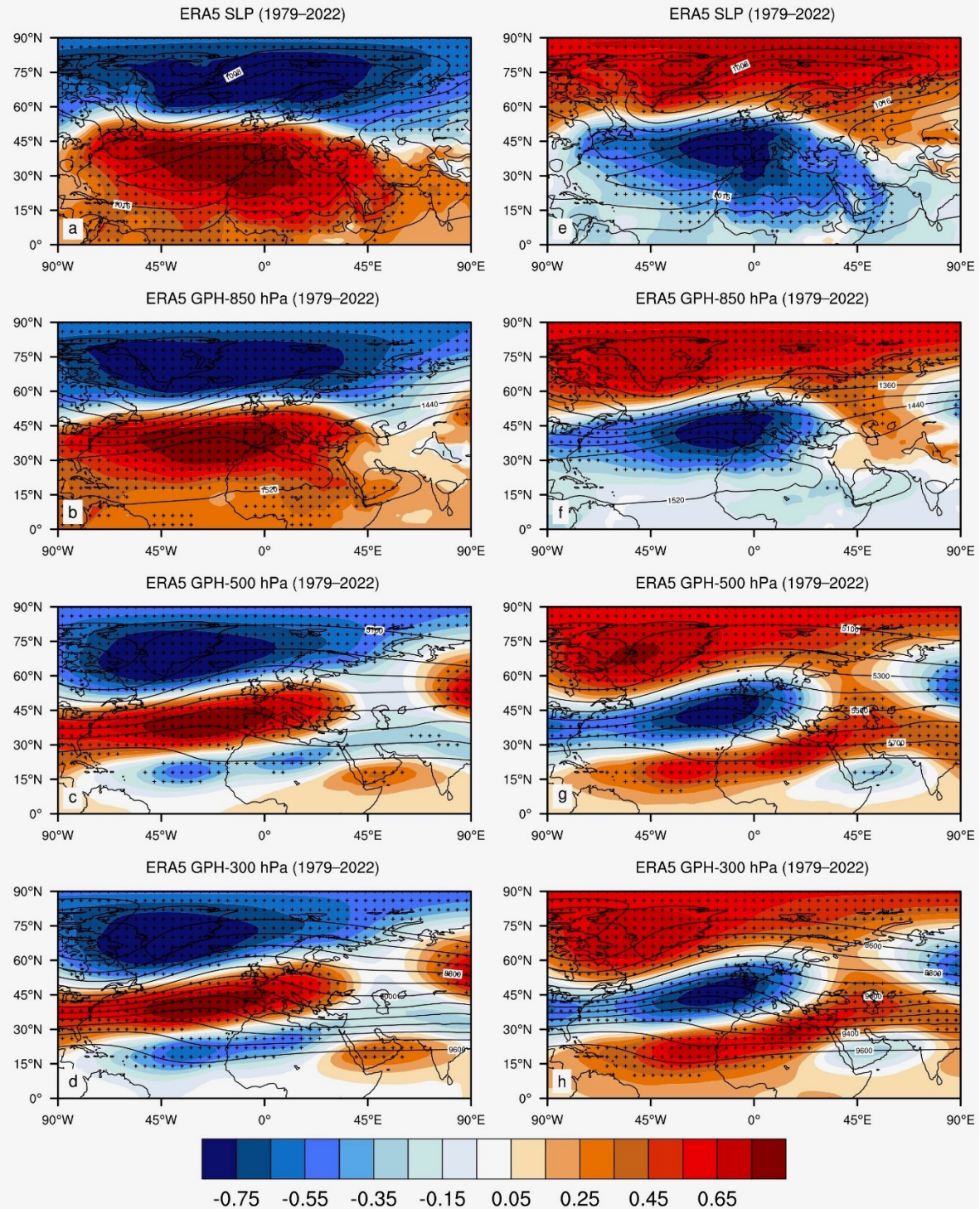

Fig. 4. *Spatial patterns of correlation (shading in color) between NAOI (Fig. 2) and (a) SLP (hPa), and (b)–(d) GPH (m) at 850, 500, and 300 hPa for the period 1979–2022 from the ERA5. Stippling indicates that the correlation coefficient is statistically significant at the 5% level ($p < 0.05$). The contour lines in black indicate the climatological values of SLP in (a) and GPH in (b)–(d). (e)-(h) are the same as (a)-(d) except for the correlation with the observed STI (Fig. 3).*

3.2. Large-scale teleconnection patterns on much longer time scales

For comparison and validation, in this subsection we will perform similar analyses as done above but on much longer time scales. For the observational temperatures, our analysis goes back to 1880, before which there are not adequate observations to make accurate temperature estimation. For the reanalysis data, our analysis goes back as far as 1864 when the UCAR NAOI becomes first available. We compare the results from the satellite era to those from several century-long datasets and account for uncertainties in observations and differences in construction methods (Dalelane et al., 2023). It is essential that similar teleconnection patterns in section 3.1 can be reproduced by the century-long datasets if the NAO is the dominant contributor to the Saharan temperature interannual variability.

Figure 5 shows interannual variations in STI averaged from 53 weather stations over the Sahara from the GHCNMv4, together with the NOAA and NCAR NAOI (Fig. 1b). Despite strong interannual and decadal variations, the temperatures is significantly correlated negatively with the NCAR NAOI for the period 1880-2022 ($R=-0.71$, $p < 0.001$) and the NOAA NAOI for the period 1950-2022 ($R=-0.82$, $p < 0.001$). Evidently, these correlations are similar in sign and comparable in magnitude to those in the satellite era (Fig. 2).

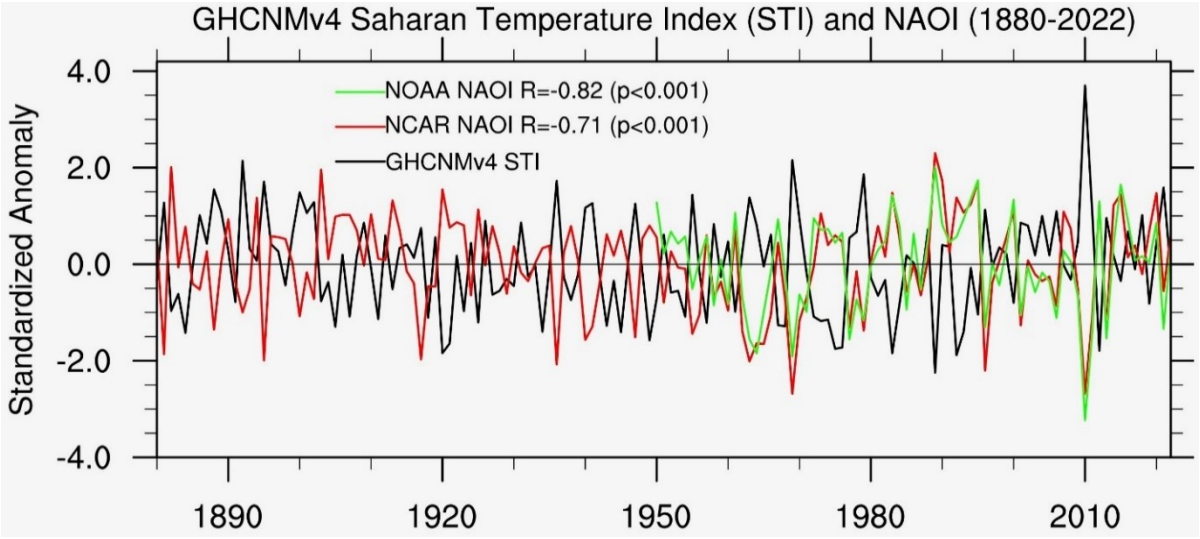

Fig. 5. *Interannual variations in standardized NAOI and STI for the period 1880–2022 from the GHCNMv4, where there are 53 weather stations over the inner domain of the Sahara Desert*

(20°N–30°N, 15°W–35°E) used to calculate the STI. The correlation (R) and its significance level (p value) between the two NAOI and STI are shown.

Note that there is a strong and significant correlation (R=0.97, p < 0.001) between the two NAOI for the overlapping period 1950-2022 (Fig. 1b), which is slightly larger than that in the satellite era (R=0.92, p < 0.001; Fig. 1a), indicating great similarity and consistency between these two NAOI datasets. The NCAR NAOI (Fig. 1b) is mainly used next to represent the observed NAOI due to its long data record.

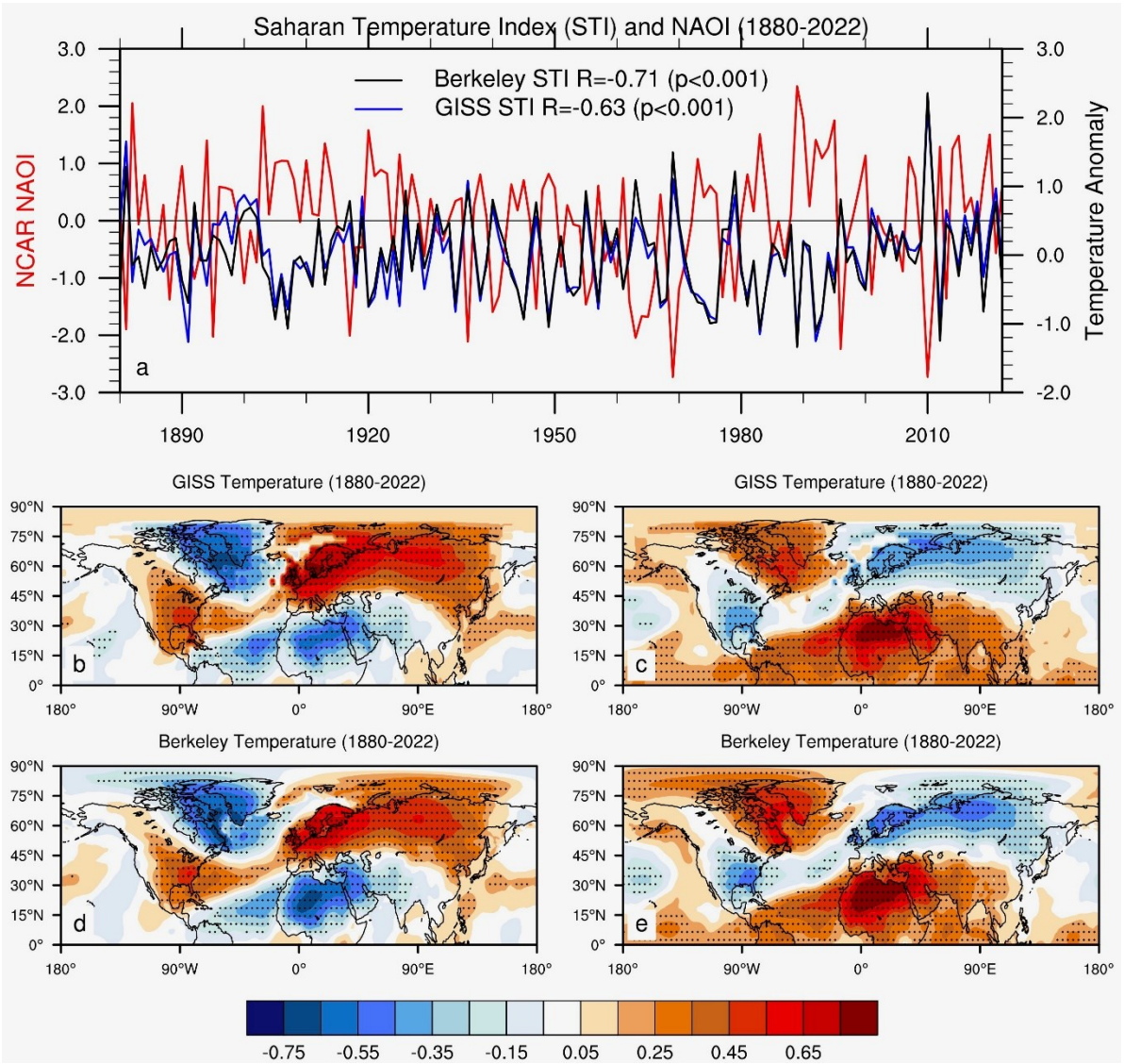

Fig 6. (a) Interannual variations in standardized NCAR NAOI and STI for the period 1880–2022 from the GISS and Berkeley. The correlation (R) and its significance level (p value) between NAOI and STI are shown. (b, d) Spatial patterns of correlation between the NCAR NAOI and surface temperature for the period 1880–2022 from (b) GISS and (d) Berkeley. (c, e) are the same as (b,

d) except for the correlation with the STI. Stippling indicates that the correlation coefficient is statistically significant at the 5% level ($p < 0.05$).

Figure 6a illustrates interannual variations in STI from the GISS and Berkeley, together with the NCAR NAOI for the period 1880-2022. Like Fig. 5, the NAOI correlates strongly and significantly with the temperatures from the GISS ($R=-0.63$, $p < 0.001$) and Berkeley ($R=-0.71$, $p < 0.001$). The spatial patterns of correlation between NCAR NAOI and surface temperatures from the GISS (Fig. 6b) and Berkeley (Fig. 6d) exhibit large-scale teleconnection patterns similar to those during the satellite era (Figs.3a-c), except small regional differences. For example, the tripolar pattern in the NAOI-SST correlations over the North Atlantic (Figs 6b and 6d) are similar to that in Figs. 3a-c but the correlations in the subtropics are much weaker in magnitude and smaller in spatial extent; the widespread negative correlations over northern Africa, the Middle East, and southwestern Asia are comparable to those in Figs. 3a-c. As expected, the spatial patterns of correlation between STI and surface temperatures from the GISS (Fig. 6c) and Berkeley (Fig. 6e) are almost identical to those in Figs. 6b and 6d except with opposite signs. Again, the nearly perfect spatial correspondence with opposite correlations between Figs. 6b and 6d and Figs. 6c and 6e reaffirm the dominant role of the NAO in influencing the Saharan interannual temperature variability on much longer time scales.

Figure 7a shows interannual variations in STI from the 20CRv3 and NCAR NAOI for the period 1864-2015. Despite strong interannual and decadal variations, the NAOI is significantly correlated negatively with the ensemble mean STI ($R=-0.76$, $p < 0.001$). As the 20CRv3 only provides the ensemble mean and spread, individual ensemble member reanalyses cannot be examined. However, the time-varying ensemble spread is very small in comparison to the ensemble mean and so will not modify the overall strong negative correlation. The spatial patterns of correlation of ensemble mean surface temperatures with the NCAR NAOI (Fig. 7b) and STI (Fig. 7c) exhibit similar large-scale teleconnection patterns as observed (Figs 6b-e).

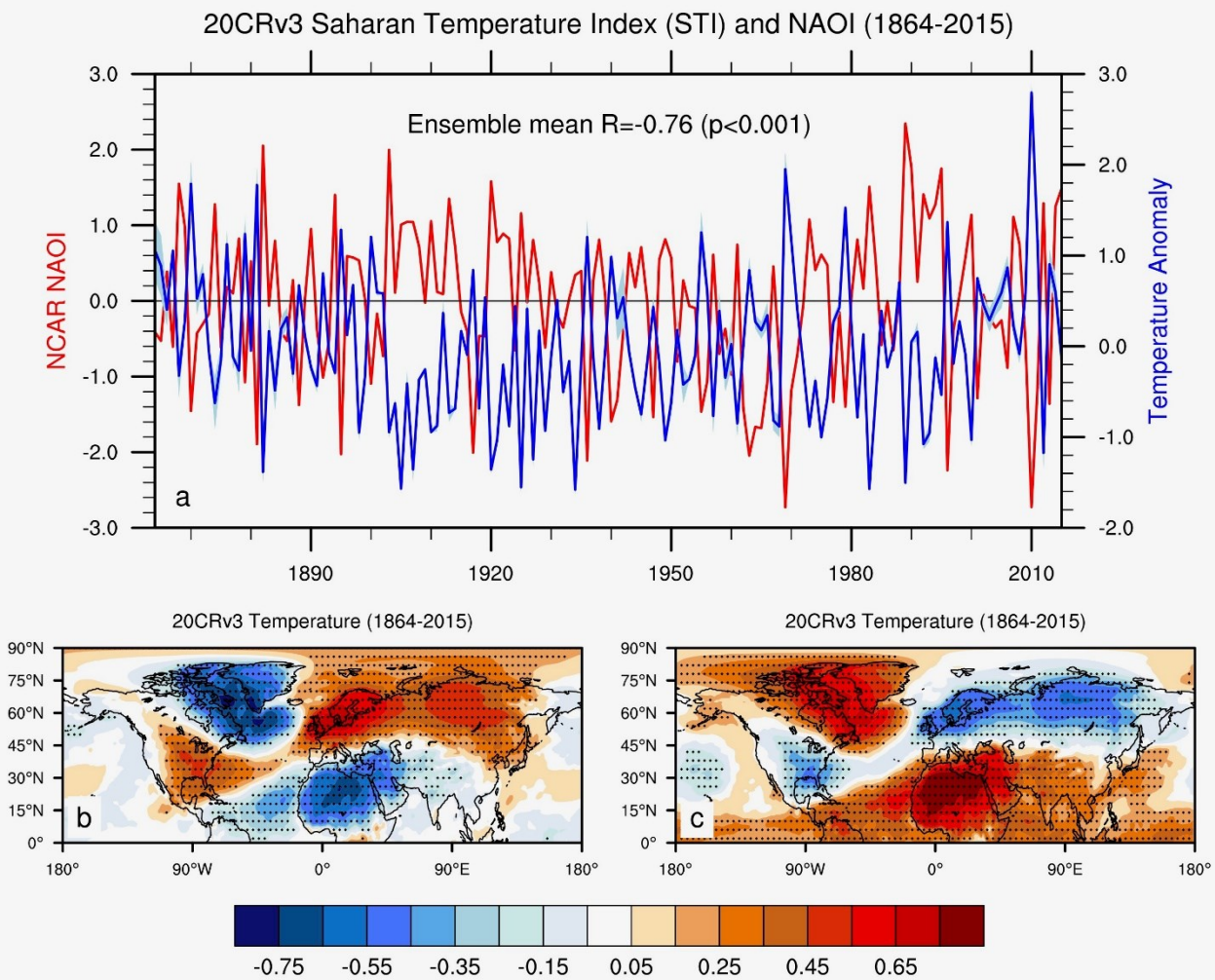

Fig 7*. (a) Interannual variations in standardized NCAR NAOI and STI for the period 1864–2015 from the 20CTv3 80-member ensemble mean and its one standard deviation (STD). The correlation (R) and its significance level (p value) between NAOI and STI are shown. (b) Spatial patterns of correlation between the NCAR NAOI and surface temperature during DJFM for the period 1864–2022 from the 20CTv3 ensemble mean. (c) is the same as (b) except for the correlation with the STI. Stippling in (b) and (c) indicates that the correlation coefficient is statistically significant at the 5% level (p < 0.05).*

Figure 8a displays interannual variations in STI from the CERA-20C and the NCAR NAOI for the period 1901-2010. Like Fig. 7a, despite strong interannual and decadal variations, the NAOI corelates significantly with the ensemble mean STI (R=−0.76, p < 0.001). The 10 ensemble member analyses can be used to assess the ensemble spread for this correlation to better account for errors in the forecast model and uncertainties in the observational data assimilation. The ensemble spread in the CERA-20C gradually decreases over time, indicating increased confidence in the reanalysis state as the quantity and quality of assimilated observations improve with time

575 (Dai and Wright, 2021). Overall, the time-varying ensemble spread is relatively small in
576 comparison with the ensemble mean and so the correlations of NAOI with the individual members
577 and the ensemble mean range between -0.77 and -0.79, with all being statistically significant
578 ($p<0.001$). The small ensemble spread indicates that uncertainties in observations and differences
579 in construction methods have a minor role in affecting the Saharan temperature variability. Again,
580 the spatial patterns of correlation of ensemble mean surface temperatures with the NCAR NAOI
581 (Fig. 8b) and STI (Fig. 8c) exhibit similar large-scale teleconnection patterns as observed (Figs.
582 6b-e).
583

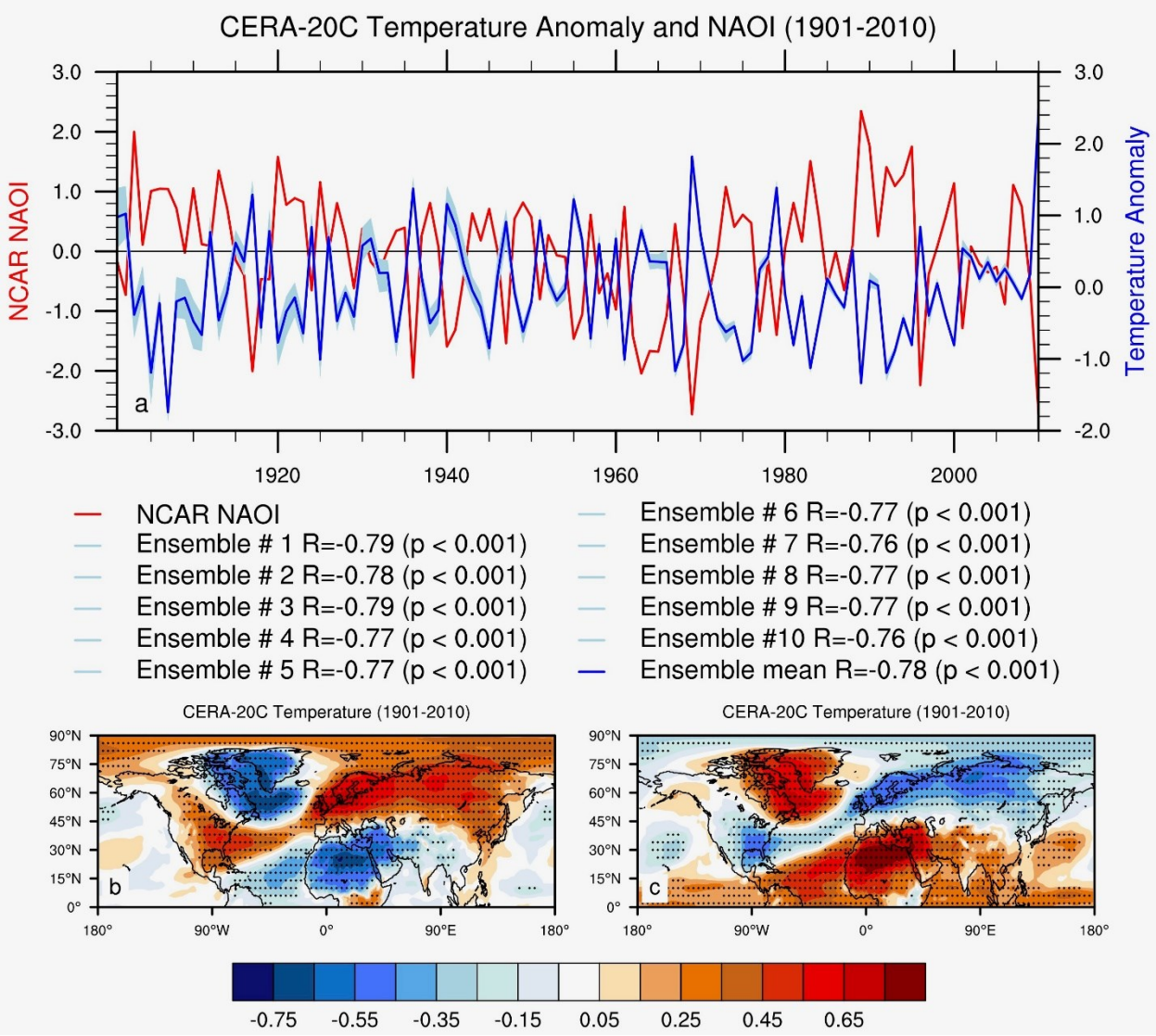

584

585 ***Fig. 8***. *Same as Fig.7 except for the 10-member ensemble reanalyses and their ensemble mean*
586 *from the CERA-20C.*

In this subsection, we have compared the time evolution of teleconnection patterns of the NAO with temperatures from three observational datasets (GISS, Berkely and GHCNMv4) and two century-long reanalyses (20CRv3 and ERA20C) on much longer time scales. All datasets contain strong interannual and decadal (and multi-decadal) variability and show the maximum temperature anomalies along with the minimum NAOI in 2010 during the entire study periods. Despite some small discrepancies at regional scales, the large-scale teleconnection patterns, particularly over the North Atlantic–Sahara sector, are similar and consistent among different datasets and between the satellite era and century-long periods. The broadly similar teleconnection patterns across different datasets and the small ensemble spread among individual ensemble members affirm that data uncertainties play a much smaller role than the NAO in controlling the Saharan temperature interannual variability.

3.3. Regional-scale teleconnection patterns during the satellite era

In this subsection we use the ERA5 reanalysis dataset for the period 1979–2022 to examine the three-dimensional structure of the NAO teleconnection over the Sahara and surrounding areas by focusing on six key variables in the troposphere: GPH, specific humidity (q), temperature (T), and the three wind components (u, v, and ω). Note that the average standardized NAOI from the two indices (NCAR and NOAA) is used to represent the observed NAOI here.

First, we analyze the spatial patterns of circulation anomalies, as well as T and q anomalies, associated with the NAO phases. The SLP and the GPH at 850 hPa (GPH at 500 hPa and 300 hPa) exhibit similar correlation patterns (Fig. 4), so that SLP (GPH at 300 hPa) will be used to illustrate the spatial features at the surface (in the upper troposphere) in the remainder of this paper.

Figures 9a and 9b illustrate the spatial patterns of climatological circulation patterns at the surface and 300 hPa, respectively, over the Sahara and surrounding areas, so that the composite anomalies shown hereafter over this region may be placed in proper context. At the surface (Fig. 9a), the subtropical Azores High is centered at 35ºN, 28ºW and extends over much of the Sahara, with clockwise flow around the subtropical anticyclone. Correspondingly, the northeast trade winds

dominate much of northern Africa. The Azores High is replaced by a ridge over the subtropical North Atlantic at 300 hPa (Fig. 9b), where strong westerlies dominate latitudes spanning 10ºN–60ºN.

Figures 9c and 9d show the spatial patterns of composite anomalies in wind at the surface and SLP, and in wind and GPH at 300 hPa, respectively, for the NAO−. Evidently, a cyclonic wind anomaly field accompanied by a negative SLP/GPH anomaly field weakens the anticyclonic flow centered over the Azores High in the climatology plot at the surface and in the upper troposphere. Negative anomalies in SLP in Fig. 9c create southwesterly wind anomalies over the entire Sahara at the surface, while positive anomalies in GPH in Fig. 9d create northeasterly wind anomalies over the southern and eastern portions of the Sahara in the upper troposphere.

Figures 9e-f show the spatial patterns of composite anomalies in wind at the surface and SLP, and in wind and GPH at 300 hPa, respectively, for the NAO+. In contrast to Figs. 9c-d, an anticyclonic wind anomaly field accompanied by a positive SLP/GPH anomaly field strengthens the anticyclonic flow centered over the Azores High in the climatology at the surface and in the upper troposphere. Positive anomalies in SLP in Fig. 9e create northeasterly wind anomalies over the entire Sahara at the surface, while negative anomalies in GPH in Fig. 9f create southwesterly wind anomalies over the southern and eastern portions of the desert in the upper troposphere.

The composite anomalies in SLP are statistically significant ($p < 0.10$) based on Monte Carlo simulation over almost the entire domain including the Sahara for both NAO phases (Figs 9c and 9e). Interestingly, the composite anomalies in GPH are statistically significant ($p<0.10$) over much of the study domain including the Sahara for the NAO− (Figs 9d), but only over the northern Atlantic Ocean, Europe and the northwestern Sahara for the NAO+ (Figs 9f). This spatial asymmetry in the composite anomalies between the two NAO phases is only evident at 300 hPa, not at the surface.

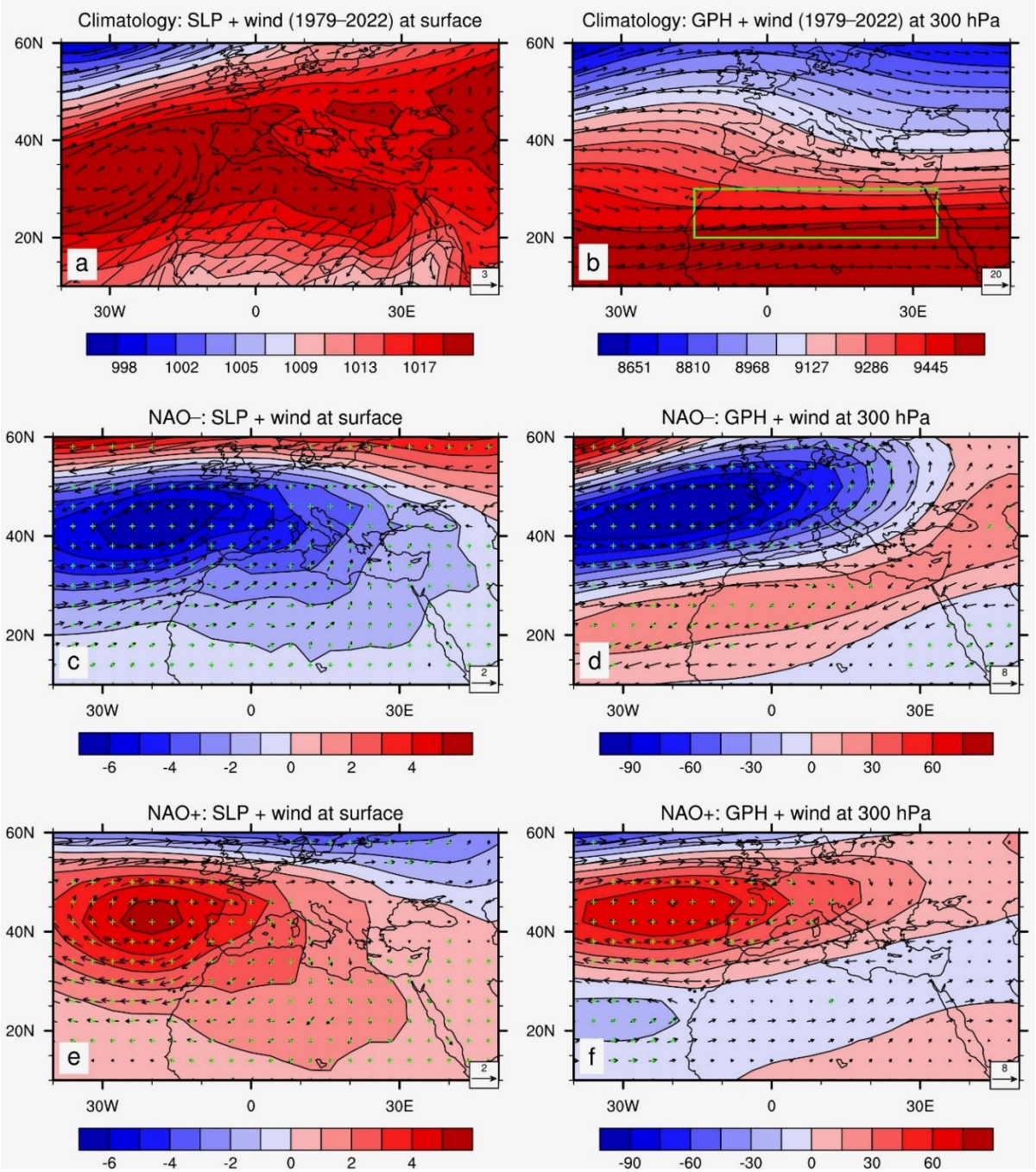

Fig. 9. *Spatial patterns of (a) climatological wind (vector, m s^{-1}) at the surface and SLP (shading, hPa) and (b) climatological wind (vector, m s^{-1}) and GPH (shading, m) at 300 hPa for the period 1979–2022 over the Sahara and surrounding regions from the ERA5. Panels (c) and (d) are the same as (a) and (b) except for the composite anomalies during the NAO−. Panels (e) and (f) are the same as (c) and (d) except for the composite anomalies during the NAO+. Stippling (with green cross symbol) indicates that the composite anomaly in SLP/GPH is statistically significant ($p<0.10$) based on Monte Carlo simulation. The green rectangle (20°N–30°N, 15°W–35°E) depicted in Fig. 9b represents the inner domain of the Sahara Desert where regional mean quantities are calculated.*

Figure 10 displays the spatial patterns of climatology and composite anomalies of q and T at the surface and 300 hPa for the NAO− and NAO+ over the Sahara and surrounding areas. Note that, as expected, the climatology and composite anomalies of q at 300 hPa are very small, but are shown to be consistent with corresponding surface plots and not considered in the following discussion of Fig. 10. For the surface climatology (Fig. 10a), north–south and land–sea thermal contrasts are evident, particularly in middle latitudes, with the Sahara bordering warmer and moister air over the North Atlantic Ocean to the west and colder and drier air over higher latitudes to the north. For the NAO− (Fig. 10c), cold and dry anomalies are seen over southern Europe and the subtropical North Atlantic where the Azores High is centered, while warm and moist anomalies are seen over the tropical North Atlantic, northern Africa, and the Middle East. In general, most of the surface T anomalies > 0.35ºC or < -0.35ºC, which cover the entire Sahara and Europe for both NAO phases, and the tropical and subtropical northern Atlantic (tropical and subpolar northern Atlantic) for the NAO− (NAO+), are statistically significant ($p < 0.10$). For the climatology at 300 hPa (Fig. 10b), the land–sea thermal contrast is much weaker but the north–south temperature gradient is more visible than in the climatology at the surface (Fig. 10a). For the NAO− at 300 hPa (Fig. 10d), cold anomalies are seen over much of the middle latitudes extending to the subtropical North Atlantic where the Azores High is centered, but to the south of the Azores High warm anomalies are seen from the North Atlantic between 15ºN and 30ºN to the northwestern Sahara. Cold anomalies also are seen at 300 hPa from the eastern Sahara to the Middle East between 20ºN and 35ºN and between 15ºE and 50ºE. As expected, the NAO− (Figs. 10c and 10d) exhibits opposite-signed anomaly patterns from the NAO+ (Figs. 10e and 10f) for T and q at the surface and T at 300 hPa. At the surface, the large positive and negative anomalies in T and q exhibit a southwest–northeast-oriented configuration and are confined to much of the Sahara (Figs. 10c and 10e). At 300 hPa, the large positive and negative anomalies in T also exhibit a southwest–northeast-oriented configuration but are confined to the northwestern Sahara (Figs. 10d and 10f). In general, most of the 300 hPa T anomalies > 0.45ºC or < -0.45ºC, which cover much of middle latitudes (40ºN-60ºN), the northwestern Sahara, and the subtropical Northern Atlantic for both NAO phases, are statistically significant ($p < 0.10$).

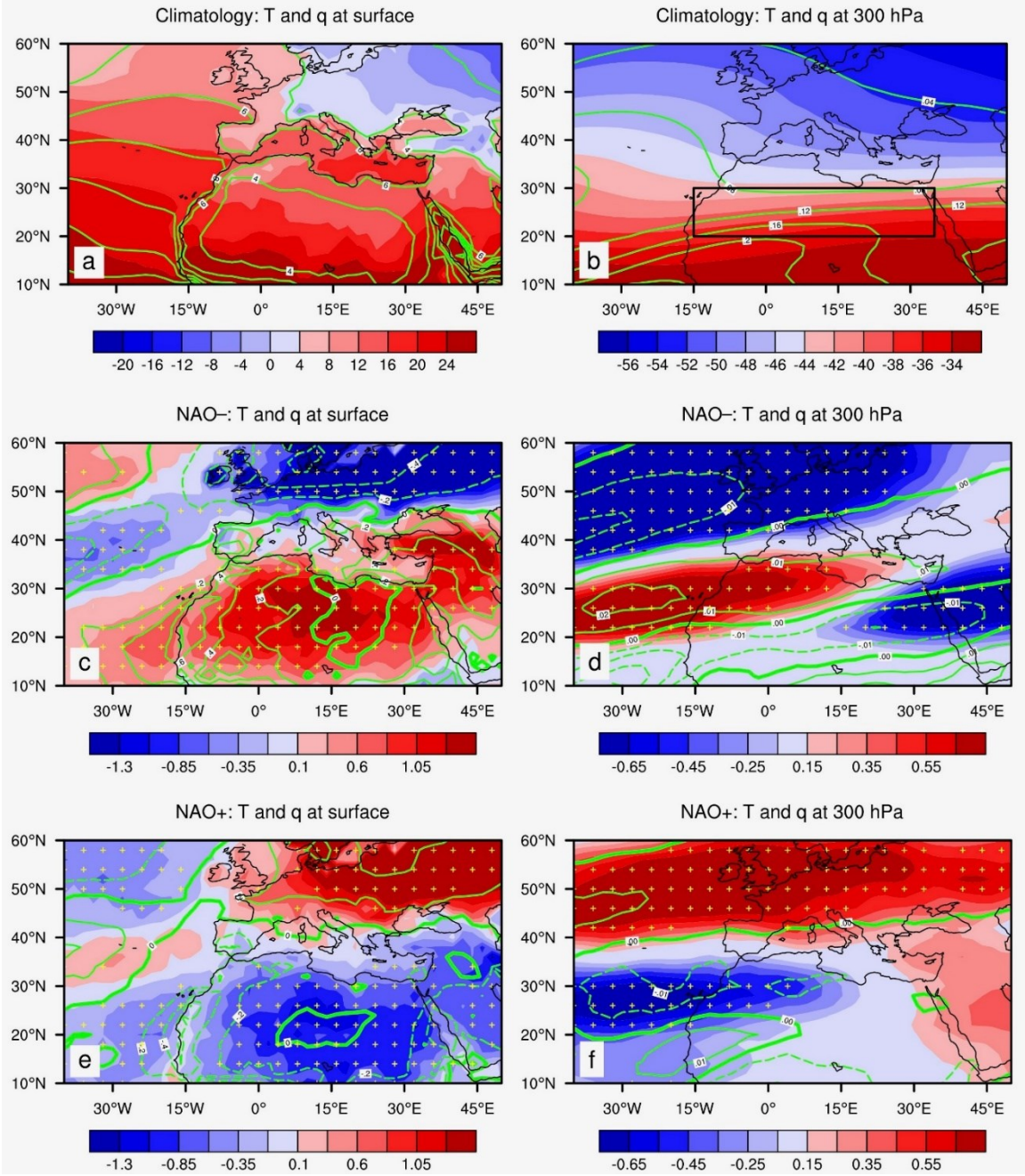

Fig. 10. *Spatial patterns of climatology (top two panels) and composite anomalies (lower four panels) of specific humidity (q, contour in green, g kg^{-1}) and temperature (T, shading, ºC) at (a), (c), and (e) the surface and (b), (d), and (f) 300 hPa for the NAO− (c) and (d) and NAO+ (e) and (f) over the Sahara and surrounding regions from the ERA5. Stippling (with yellow cross symbol) indicates that the composite anomaly in T is statistically significant ($p<0.10$) based on Monte Carlo simulation. Note that the climatology and composite anomalies of q at 300 hPa are very small but are shown for visual comparison with the corresponding surface plots. The black rectangle (20ºN–30ºN, 15ºW–35ºE) depicted in Fig. 10b represents the inner domain of the Sahara Desert where regional mean quantities are calculated.*

Next, we examine the vertical structure of several key variables associated with the NAO averaged over the inner domain of the Sahara Desert (20ºN–30ºN, 15ºW–35ºE) to highlight the regional mean features.

Figure 11 shows vertical profiles of correlations for the NAOI and STI with the regional mean anomalies in GPH, q, T, u, v, and ω averaged over the inner domain of the Sahara. The NAOI–GPH correlation changes sign with pressure from the lower to upper troposphere, with statistically significant positive (negative) correlations from 1000 to 850 hPa (500 to 200 hPa) (Fig. 11a), while the NAOI correlates negatively with q through the troposphere (Fig. 11b) and with T throughout most of the troposphere (Fig. 11c). The NAOI correlations with q (T) decrease in magnitude with decreasing pressure and are mostly statistically insignificant (significant). Like GPH, u and v show opposite-signed correlations from the lower to upper troposphere. The NAOI is associated with negative (positive) correlations below (above) 450 hPa in u (Fig. 11d) and below (above) 600 hPa in v (Fig. 11e), and most of the correlations are large and statistically significant only in the lower and upper troposphere. Like q, the NAOI correlation with ω is relatively small and mostly statistically insignificant (Fig. 11f). As expected, the NAOI and STI exhibit opposite-signed correlations with these six variables, although the vertical distributions of statistical significance of the correlations differ to some extent.

Figure 12 shows vertical profiles of regional mean composite anomalies in GPH, q, T, u, v, and ω averaged over the inner domain of the Sahara for the NAO− and NAO+. The NAO− is associated with negative (positive) GPH anomalies below (above) 700 hPa (Fig. 12a), positive (negative) q anomalies below (above) 600 hPa (Fig. 10b), and positive (negative) T anomalies below (above) 300 hPa (Fig. 12c). The anomalies in GPH have a bottom-heavy vertical profile with two maxima at 1000 hPa and 200 hPa, and the anomalies in q and T exhibit a bottom-heavy vertical structure, with the largest anomalies at 1000 hPa. Like GPH, u and v show opposite-signed anomalies from the lower to upper troposphere. The NAO− is associated with positive (negative) anomalies below (above) 550 hPa in u (Fig. 12d) and below (above) 700 hPa in v (Fig. 12e), corresponding to southwesterly (northeasterly) wind anomalies below 700 hPa (above 550 hPa). In contrast, the NAO+ exhibits opposite-signed anomalies in GPH, q, T, u, and v from the NAO−. The ω anomalies are negative (positive) below 550 hPa (between 550 hPa and 200 hPa) for the NAO−

and positive throughout the troposphere for the NAO+ (Fig. 12f), with the largest ω anomalies in the lower-to-middle troposphere. In general, despite some small differences, the vertical distributions of statistical significance ($p<0.10$) of the composite anomalies for each variable are broadly similar to the vertical distributions of statistical significance ($p<0.05$) of correlations in Fig. 11.

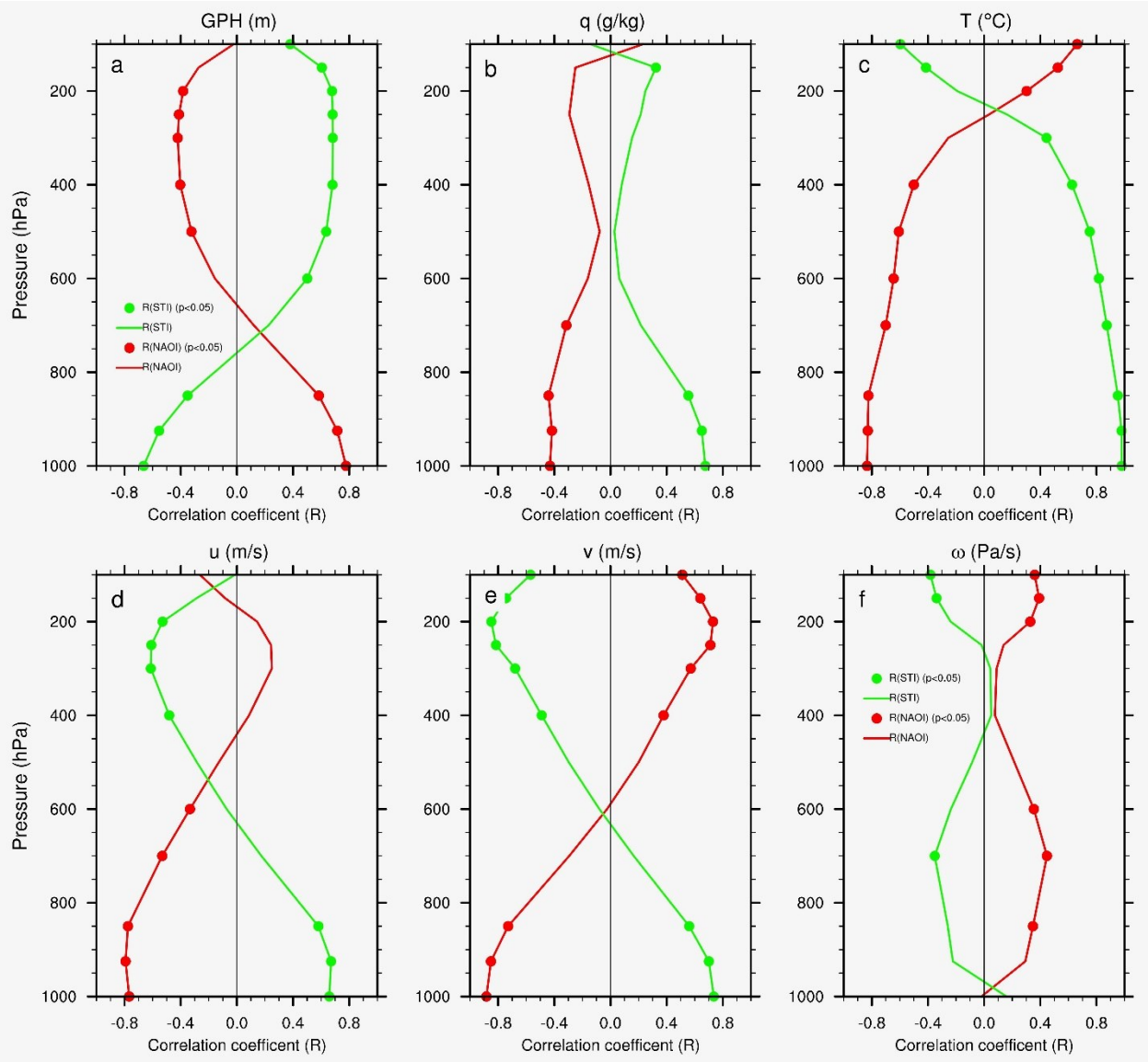

Fig. 11. *Vertical profiles of correlation for the NAOI (in red) and observed STI (in green; Fig 3) with the regional mean anomalies in (a) GPH, (b) q, (c) T, (d) u, (e) v, and (f) ω, averaged over the inner domain of the Sahara Desert (20°N–30°N, 15°W–35°E) for the period 1979–2020 from the ERA5. The correlations (in circle) are statistically significant ($p < 0.05$).*

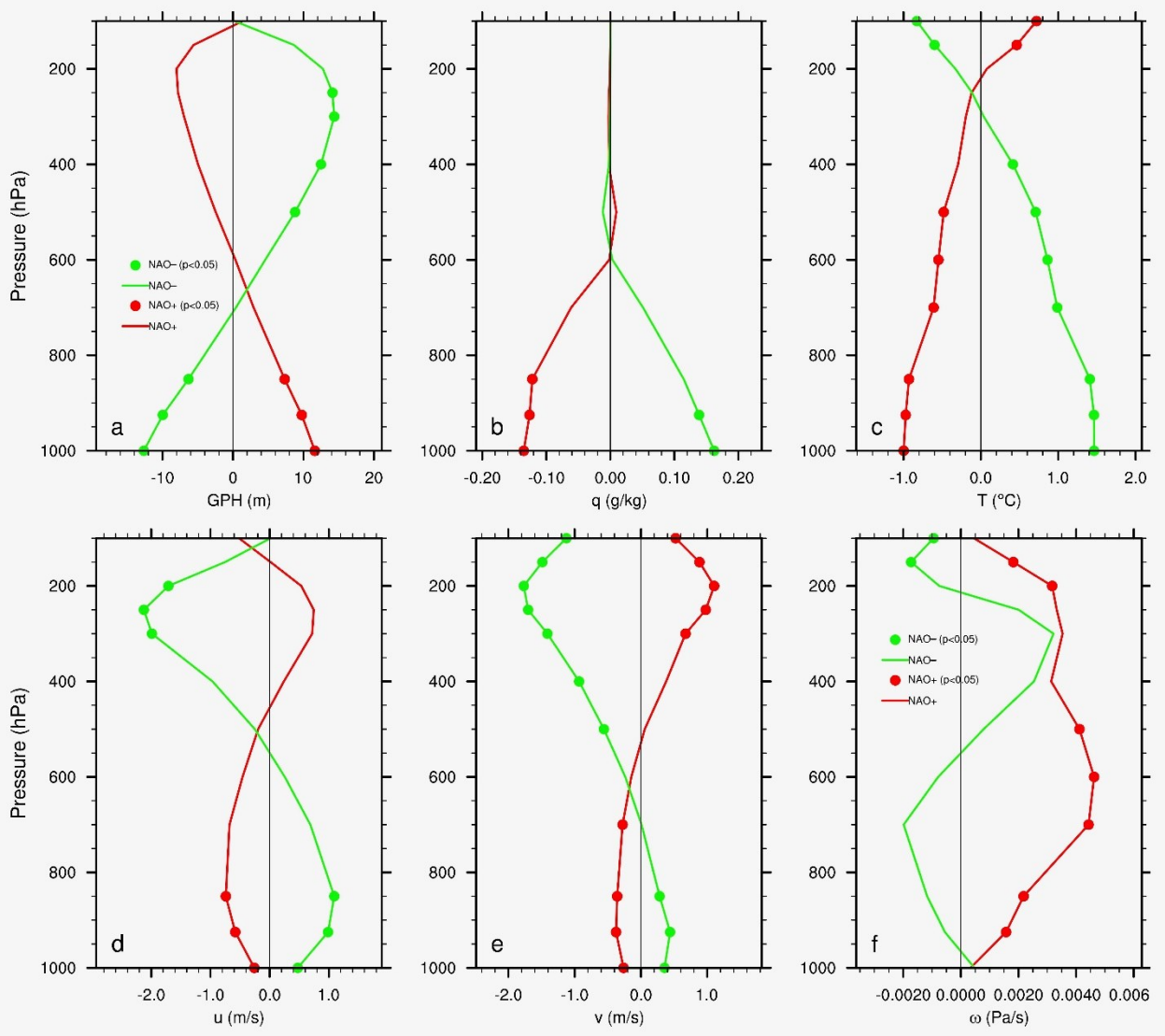

Fig. 12. *Vertical profiles of regional mean composite anomalies in (a) GPH, (b) q, (c) T, (d) u, (e) v, and (f) ω, averaged over the inner domain of the Sahara Desert (20°N–30°N, 15°W–35°E) for the NAO− (in green) and NAO+ (in red) from the ERA5. The composite anomaly (in circle) is statistically significant (p<0.10) based on Monte Carlo simulation.*

Figure 13 shows vertical profiles of regional mean absolute values for the three wind components (u, v, and ω) averaged over the inner domain of the Sahara for the climatology and the composites of the NAO− and NAO+. It aims to provide the magnitude of wind anomalies relative to the climatological wind values. The climatological mean flow consists of weak northeasterlies near the surface and transitions into strong westerlies with a weak southerly flow in the upper troposphere (Figs. 13a and 13b). As expected, the climatological large-scale subsidence is widespread across the Sahara (Fig. 13c). A major feature in the upper atmosphere is the subtropical

jet stream for the zonal mean wind with the maximum speed of 40.9 m s^{-1} centered around 200 hPa (Fig. 13a) and the southerly wind for the meridional mean wind with the maximum speed of 4.4 m s^{-1} at 200 hPa (Fig. 13b). In contrast, the wind speed is much weaker in the lower troposphere and near the surface. Relative to the climatology, the u composites indicate weaker easterly (westerly) wind in the lower (upper) troposphere for the NAO− and stronger easterly (westerly) wind in the lower (upper) troposphere for the NAO+ (Fig. 13a), with the composite anomalies below 800 hPa for both NAO phases and between 300 and 200 hPa for the NAO− being statistically significant ($p<0.10$); the v composites show weaker northerly (southerly) wind in the lower (upper) troposphere for the NAO− and stronger northerly (southerly) wind in the lower (upper) troposphere for the NAO+ (Fig. 13b), with almost all of these composite anomalies being statistically significant ($p<0.10$). For the ω composites, relative to the climatology, subsidence is slightly enhanced through the troposphere for the NAO+, while it is slightly weakened between 550 hPa and 925 hPa and enhanced between 550 hPa and 200 hPa (Fig. 13c). The ω anomalies below 500 hPa and above 200 hPa for the NAO+ are statistically significant ($p<0.10$), while the ω anomalies for the NAO− are insignificant ($p>0.10$) for all layers except 100 hPa.

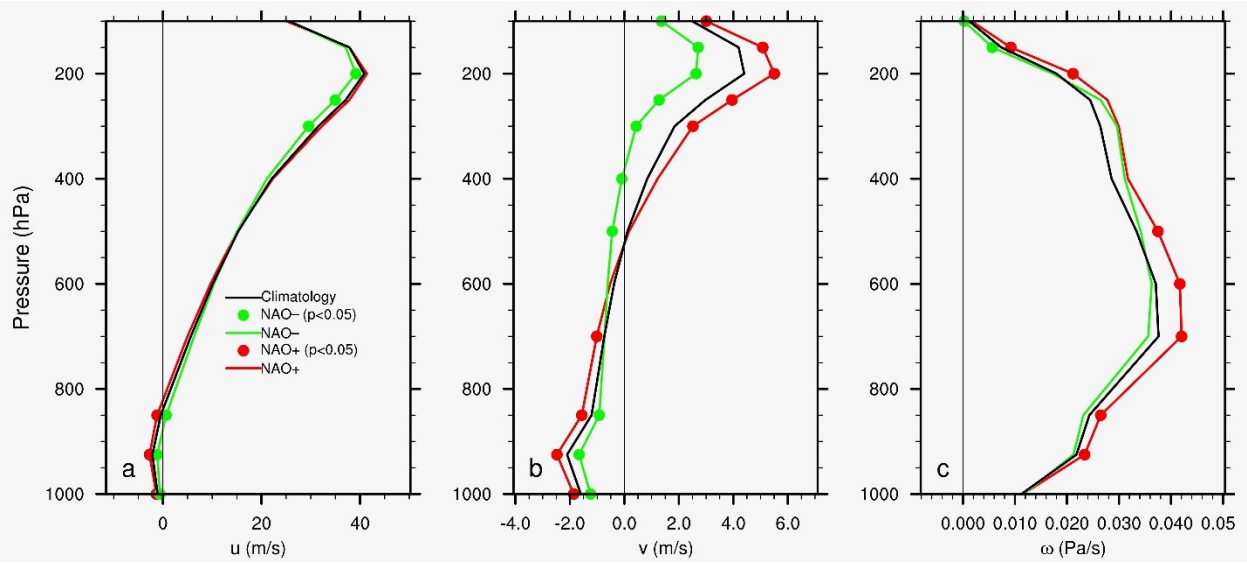

Fig. 13. *Vertical profiles of regional mean absolute values for the wind component in (a) u, (b) v, and (c) ω, averaged over the inner domain of the Sahara Desert (20°N–30°N, 15°W–35°E) for the long-term climatology (in black) and the composites of NAO− (in green) and NAO+ (in red) from the ERA5. The composite value (in circle) is statistically significant ($p<0.10$) from the climatology based on Monte Carlo simulation.*

It is worth noting that the upper-tropospheric anomalies (Figs. 11-13) may have stratospheric links as there is a strong dynamic coupling between the stratospheric and tropospheric circulations (e.g., Hurrell et al., 2003; Thompson et al., 2003; Pinto and Raible, 2012; Nigam and Baxter, 2015). As the focus of this study is on the troposphere and so this connection will not be explored here.

The results in this subsection indicate that the NAO teleconnection is significantly linked with the large-scale circulation anomalies in the troposphere over the Sahara and its surrounding areas. The composite analysis reveals clearly opposite-signed changes in GPH, u, and v from the lower to upper troposphere over the Sahara (Figs. 11-13). The NAO− (NAO+) exhibits warmer and moister (colder and drier) air than normal in the lower troposphere, southwesterly (northeasterly) wind anomalies in the lower troposphere and northeasterly (southwesterly) wind anomalies in the upper troposphere (Figs. 9-10), and slightly weaker (stronger) subsidence anomaly between 925 hPa and 550 hPa (Figs. 11-13). In particular, during the NAO− (NAO+) the southwesterly (northeasterly) wind anomalies in the lower troposphere over the Sahara help to advect warmer and moister (colder and drier) air over the North Atlantic (northern higher latitudes) to the Sahara, which may mainly explain the above-normal (below-normal) Saharan temperatures (see more discussion in next section).

3.4. Possible mechanisms of NAO impacts on the Saharan temperatures

Past studies have concluded that SAT anomaly patterns for both positive and negative NAO phases are mainly driven by horizontal temperature advection (e.g., van Loon and Rogers, 1978; Rogers and van Loon, 1979; Wallace and Gutzler, 1981; Watanabe, 2004; Woollings et al., 2008; Hurrell et al., 2003; Nigam and Baxter, 2015). To attribute the NAO impacts on both surface and atmospheric temperature anomalies, Clark and Feldstein (2020a; 2020b) conducted a comprehensive composite analysis of the thermodynamic energy equation over the NH using ERA-Interim reanalysis, and included a detailed analysis of all major heating processes over four selected regions, including northern Africa. By combining their analyses with our results presented in previous sections, the major physical mechanisms in explaining the NAO impacts on the Saharan surface and tropospheric temperatures are synthesized as follows. In the lower troposphere and near the surface where climatological wind speeds are small, but the anomaly winds are

relatively large in magnitude (Figs. 9, 12-13), advection of climatological warm and moist (cold and dry) air over the North Atlantic (northern higher latitudes) by the anomalous southwesterly (northeasterly) wind result in above-normal (below-normal) temperatures over the Sahara during the NAO− (NAO+) (Figs. 10, 12-13). In the upper troposphere where climatological wind speeds are large but anomalous northeasterly (southwesterly) winds are relatively small in magnitude (Figs. 9, 12-13), the anomalous North Atlantic warm (cold) air advected by climatological strong westerlies explain well the warming (cooling) over the Sahara during the NAO− (NAO+) (Figs. 10, 12-13). Such advection mechanisms are illustrated in the schematic of Fig. 14.

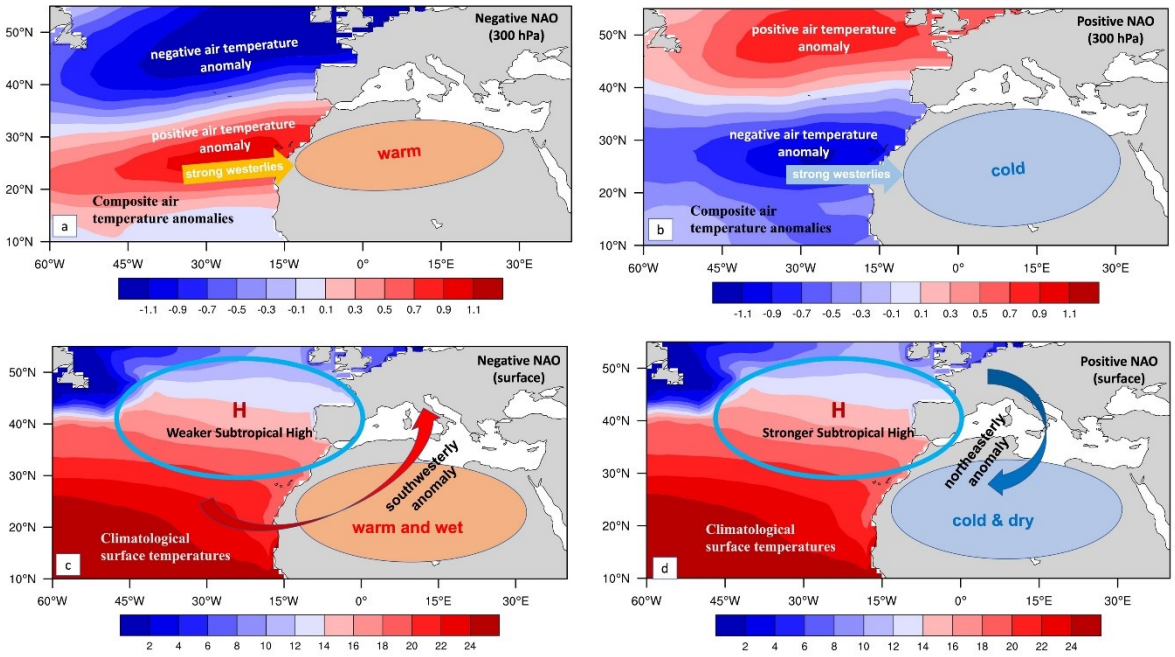

Fig. 14. *Schematic of mechanisms of NAO impacts on the Saharan interannual temperature anomalies at (a), (b) 300 hPa and (c), (d) the surface for (a), (c) NAO− and (b), (d) NAO+. Shading represents (a), (b) composite air temperature anomalies (ºC) and (c), (d) climatological SSTs (ºC) over the North Atlantic.*

Beside the aforementioned advection mechanisms, the diabatic heating term associated with turbulence is expected to impact the Saharan interannual temperature variability as well. Over the arid subtropic deserts, the vertical turbulent mixing in the atmospheric boundary layer (PBL) is typically much stronger than other regions because more surface sensible heat flux is available to drive vertical mixing due to less surface moisture and higher Bowen ratio (Zhou, 2021; Zhou et al., 2021). At the surface where the NAO's footprint on temperature maximizes, above-normal

(below-normal) temperatures during the NAO- (NAO+) will enhance (weaken) turbulent mixing and modify vertical turbulent heat transfer over the Sahara where the strength of vertical mixing is significantly positively correlated with the magnitude of surface heating (Zhou et al., 2021; Zhou, 2021). As quantified by Clark and Feldstein (2020a; 2020b), this diabatic heating term mainly opposes the horizontal temperature advection in the lower troposphere over the Sahara.

The Sahara is formed in the subtropical subsiding branch of the Hadley cells and so generally associated with large-scale subsidence with dry and cloudless weather conditions (Zhou, 2021). Enhanced (weakened) subsidence will result in above-normal (below-normal) adiabatic warming over the Sahara. Possibly, the adiabatic heating term associated with subsidence might influence the Saharan interannual temperature variability. The subsidence over the Sahara is weakened (enhanced) slightly in the lower-to-middle troposphere during the NAO− (NAO+) but the changes in ω are small in magnitude and mostly statistically insignificant, particularly in the lowest troposphere and near the surface where the NAO-induced temperature changes are largest (Figs. 11-13). These changes in ω would result in a weak anomalous adiabatic warming/cooling term opposite in sign with the observed temperature anomaly, consistent with the conclusions in Clark and Feldstein (2020b; their Fig. 3). This implies that the adiabatic term has a limited impact on interannual variability of Saharan temperatures.

Recent studies have documented amplified warming on SAT due to enhanced downward longwave radiation associated with increased moisture content in a warming climate over the Sahara, where the air is very dry and thus extremely sensitive to changes of water vapor (Cook and Vizy 2015; Zhou et al., 2015; 2016; Zhou, 2016; Vizy and Cook, 2017; Evan et al., 2017; Wei et al., 2017). Similarly, interannual variations in atmospheric water vapor could modify the lower tropospheric temperatures via the greenhouse effects of water vapor. Figure 15 shows the spatial patterns of composite anomalies in the vertically integrated moisture flux and divergence for the NAO− (Fig. 15a) and NAO+ (Fig. 15b). The NAO-induced changes in atmospheric moisture content are very small and statistically insignificant ($p<0.10$) across the entire Sahara, except for a small portion of the northwestern Sahara, consistent with the insignificant correlation between NAOI and q for most pressure layers in Fig. 11b. These results suggest that water vapor changes associated with the NAO do not contribute significantly to downward longwave radiation anomalies over Sahara

and thus the Saharan interannual temperature variations, consistent with partial radiative perturbation calculations conducted over northern Africa for days when the NAO is active (Clark and Feldstein 2020b).

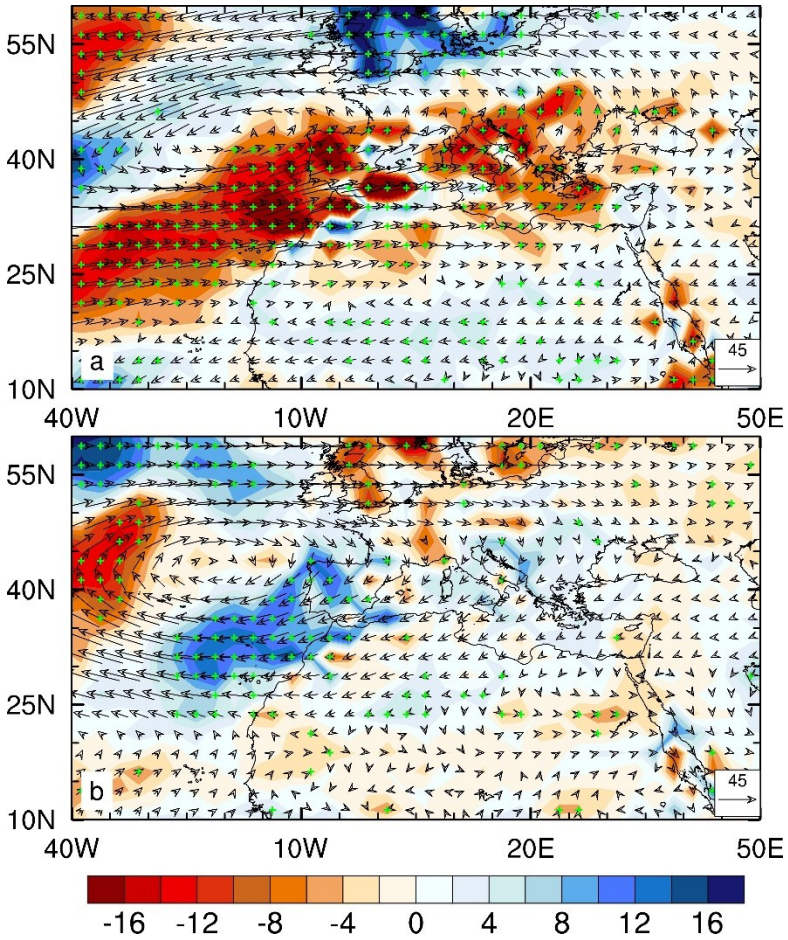

Fig. 15. *Spatial patterns of composite anomalies in the vertically integrated (from 1000 hPa to 300 hPa) moisture flux (vector, kg m^{-1} s^{-1}) and moisture flux divergence (shading, 10^{-5} kg m^{-2} s^{-1}) for the NAO− (a) and NAO+ (b) from the ERA5. Stippling (with green cross symbol) indicates that the composite anomaly in moisture flux divergence is statistically significant ($p<0.10$) based on Monte Carlo simulation.*

In summary, the NAO-induced changes in circulation and associated horizontal temperature advection are the dominant contributors to the interannual temperature variability over the Sahara. Because the Sahara is extremely arid and the vertical turbulent mixing in the PBL depends strongly on surface heating (Zhou et al., 2021), the diabatic heating term of vertical mixing is the second major modulator to this temperature variability by opposing the horizontal temperature advection

in the lower troposphere, where the enhanced (weakened) vertical mixing cools (warms) the lower PBL and warms (cools) the upper PBL during the NAO- (NAO+). Overall, the small changes in atmospheric moisture content and subsidence have a much smaller role in modifying the Saharan temperatures than the dominant effects of horizontal temperature advection and vertical mixing (Clark and Feldstein, 2020a; 2020b).

4. Conclusions

This paper uses a multidata synthesis approach to examine the NAO's influences on the Saharan temperature variability on interannual time scales based on correlation and composite analyses of multiple long-term observational and reanalysis datasets during boreal winter (DJFM) for the satellite era (1979-2022) and much longer periods. It compares the findings from the satellite era to those from several century-long observational datasets and account for errors in the forecast model and uncertainties in observations and differences in construction methods using two century-long ensemble reanalyses. It presents evidence for a solid teleconnection pattern over the Sahara associated with the NAO in surface and tropospheric temperatures and documents some major spatial-temporal and vertical characteristics of this pattern for both positive and negative NAO phases.

We find that the Saharan temperature anomalies are negatively correlated with the NAOI in all datasets and this correlation is very strong, consistent, and statistically significant, indicating an interannual teleconnection between the Saharan temperature and the NAOI. The broadly similar teleconnection patterns between different periods and across different datasets and the small ensemble spread among individual ensemble members affirm that data uncertainties play a much smaller role than the NAO in controlling the Saharan temperature variability. Our results indicate that the NAO teleconnection is significantly linked with large-scale circulation anomalies throughout the troposphere over the North Atlantic−Sahara sector, where anomalous u and v wind components and GPH fields exhibit opposite-signed changes with altitude from the lower to upper troposphere. During the NAO− (NAO+), above-normal (below-normal) temperatures over the Sahara can be mainly explained by three major processes: (1) advection of climatological warm and moist (cold and dry) air over the North Atlantic (northern higher latitudes) by the anomalous

908 southwesterly (northeasterly) flow in the lower troposphere; (2) advection of anomalous North
909 Atlantic warm (cold) air by the climatological strong westerlies in the middle and upper
910 troposphere, and (3) strengthened (weakened) turbulent mixing and thus vertical heat transfer in
911 the lower troposphere via cooling (warming) the lower PBL and warming (cooling) the upper PBL.
912 Overall, the NAO-induced anomalies in circulation and associated horizontal temperature
913 advection and vertical heat transfer via turbulent mixing mainly explain the strong surface and
914 tropospheric temperature anomalies during the NAO- and NAO+ over the Sahara.
915
916 These results suggest the NAO plays an important role in modulating the Saharan interannual
917 temperature variability. This work represents the very first comprehensive study of the NAO
918 teleconnection patterns over the largest hot desert in the world and establish their spatiotemporal
919 and vertical features. It allows for a better understanding of links between climate variations in the
920 North Atlantic Ocean and the interannual temperature variability over the Sahara in a statistical
921 framework. The focus of this study is the documentation of the NAO impacts on the Saharan
922 climate variability, not the establishment of the detailed physical mechanisms of cause and effect
923 for such impacts in a fully coupled land-ocean-atmosphere system. Identifying possible influences
924 of other climate modes such as the Arctic Oscillation (AO) (e.g., Watanabe, 2004), El Niño–
925 Southern Oscillation (ENSO) (e.g., Li and Ruan, 2018; Pausata et al., 2020), Atlantic multidecadal
926 oscillation (AMO) and Pacific decadal oscillation (PDO) (e.g., Thomas and Nigam, 2018), and
927 Indian Ocean Dipole *(*IOD) (e.g., Yamagata et al., 2004) will be explored in future work.
928
929 Various teleconnection patterns have been used to explain regional anomalous weather and
930 climate. As one of the most prominent and recurrent patterns of atmospheric circulation variability,
931 the NAO dictates climate variability over much of the NH, especially during boreal winter, and its
932 associated climate variations have profound environmental, societal, economic, and ecological
933 impacts (Hurrell et al., 2003). It has been increasingly recognized recently that the Sahara has
934 played an important role in the climate system from changes in regional atmospheric circulation
935 (e.g., the West African monsoon) to remote impacts on far-afield regions, such as the equatorial
936 Pacific or the Arctic (Knippertz and Todd, 2012; Vizy and Cook, 2017; Thomas and Nigam, 2018;
937 Pausata et al., 2020; Zhou et al., 2021; Zhou, 2021). In particular, the Sahara is currently the largest
938 source of airborne mineral dust on Earth, and the NAO has a strong control on atmospheric export

of dust from northern Africa (Moulin et al., 1997). The changes in dust load and transport in the atmosphere can contribute significantly to regional to global climate variability by altering radiation, cloud properties, atmospheric and ocean circulations (Pausata et al., 2020). Hence, understanding teleconnection patterns and major processes that control the Saharan climate variability is, therefore, of high priority and scientific significance.

Acknowledgements. We would like to thank Daniel Keyser at UAlbany for frequent discussions and extensive comments on this work. L.Z. was supported by the National Science Foundation (NSF AGS-1952745 and AGS-1854486). W.H. was supported by the National Natural Science Foundation of China (42075022). Support for the Twentieth Century Reanalysis Project version 3 dataset is provided by the U.S. Department of Energy, Office of Science Biological and Environmental Research (BER), by the National Oceanic and Atmospheric Administration Climate Program Office, and by the NOAA Earth System Research Laboratory Physical Sciences Laboratory.

References

Agrawal, S., C. R. Ferguson, L. Bosart, and D. A. Burrows, 2021: Teleconnections Governing the Interannual Variability of Great Plains Low-Level Jets in May. *J. Climate*, **34**, 4785–4802, https://doi.org/10.1175/JCLI-D-20-0451.1.

Barnston, A.G., and R.E. Livezey, 1987. Classification, seasonality and persistence of low-frequency atmospheric circulation patterns. *Mon. Wea. Rev.*, **115**, 1083-1126.

Castañeda, I. S. et al., 2009. Wet phases in the Sahara/Sahel region and human migration patterns in North Africa. *Proc. Natl Acad. Sci. USA* **106**, 20159–20163.

Chen, W. Y., and H. van den Dool, 2003. Sensitivity of teleconnection patterns to the sign of their primary action center, *Mon. Wea. Rev.*, 131, 2885-2899.

Clark, J. P., and S. B. Feldstein, 2020a. What drives the North Atlantic Oscillation's temperature anomaly pattern? Part I: The growth and decay of the surface air temperature anomalies. *J. Atmos. Sci.*, 77, 185–198, https://doi.org/10.1175/JAS-D-19-0027.1.

Clark, J. P., and S. B. Feldstein, 2020b. What drives the North Atlantic Oscillation's temperature anomaly pattern? Part II: A decomposition of the surface downward longwave radiation anomalies. *J. Atmos. Sci.*, **77**, 199–216, https://doi.org/10.1175/JAS-D-19-0028.1.

Collins, J. M., 2011. Temperature variability over Africa, *Journal of Climate*, *24*(14), 3649-3666. DOI: https://doi.org/10.1175/2011JCLI3753.1.

Cook, K. H., and E. K. Vizy, 2015. Detection and analysis of an amplified warming of the Sahara Desert. *J. Climate*, **28**, 6560–6580, https://doi.org/10.1175/JCLI-D-14-00230.1.

Copernicus Climate Change Service (C3S), 2017. ERA5: Fifth generation of ECMWF atmospheric reanalyses of the global climate. Copernicus Climate Change Service Climate Data Store (CDS), date of access. https://cds.climate.copernicus.eu/cdsapp#!/home.

Dai, L.; Wright, J.S., 2021. Long-term variability of relationships between potential large-scale drivers and summer precipitation in North China in the CERA-20C reanalysis. *Atmosphere*, *12*, 81. https://doi.org/10.3390/atmos12010081.

Dalelane, C. and Winderlich, K. and Walter, A., 2023. Evaluation of global teleconnections in CMIP6 climate projections using complex networks. Earth Syst. Dynam., 14, 17–37, https://doi.org/10.5194/esd-14-17-2023.

985 Evan, A.T., Flamant, C., Lavaysse, C., Kocha, C., Saci, A., 2015: Water vapor–forced greenhouse
986 warming over the Sahara desert and the recent recovery from the Sahelian drought. J Clim
987 28:108–123. https ://doi.org/10.1175/JCLI-D-14-00039.
988 Gelaro, R., and coauthors, 2017. The Modern-Era Retrospective Analysis for Research and
989 Applications, Version 2 (MERRA-2), *J. Clim.*, 30, 14, 5419-5454,
990 https://doi.org/10.1175/JCLI-D-16-0758.1.
991 GISTEMP Team, 2021. GISS Surface Temperature Analysis (GISTEMP), version 4. NASA
992 Goddard Institute for Space Studies. Dataset accessed 20YY-MM-DD at
993 https://data.giss.nasa.gov/gistemp/.
994 Gleixner, S., Demissie, T., Diro, G.T., 2020. Did ERA5 improve temperature and precipitation
995 reanalysis over East Africa? *Atmosphere*, *11*, 996. https://doi.org/10.3390/atmos11090996.
996 Holton, J. R., 2004. An introduction to dynamic meteorology. 4. Cambridge: Elsevier Academic
997 Press; p. 535.
998 Hurrell, J. W., and C. Deser, 2009. North Atlantic climate variability: The role of the North
999 Atlantic Oscillation. *J. Mar. Syst*., 78, No. 1, 28-41.
1000 Hurrell, J. W. & National Center for Atmospheric Research Staff (Eds). Last modified 24 Apr
1001 2020. "The Climate Data Guide: Hurrell North Atlantic Oscillation (NAO) Index (station-
1002 based)." Retrieved from https://climatedataguide.ucar.edu/climate-data/hurrell-north-atlantic-
1003 oscillation-nao-index-station-based.
1004 Hurrell, J. W., 1995. Decadal trends in the North Atlantic oscillation: regional temperatures and
1005 precipitation. *Science,* 269, 676-679.
1006 Hurrell, J. W., 1996. Influence of variations in extratropical wintertime teleconnections on
1007 Northern Hemisphere temperature, *Geophysical Research Letters*, 23 (6), 665-668.
1008 Hurrell, J. W., Kushnir, Y., Ottersen, G. and Visbeck, M., 2003. An overview of the North Atlantic
1009 Oscillation. In The North Atlantic Oscillation: Climatic significance and environmental impact
1010 (eds J.W. Hurrell, Y. Kushnir, G. Ottersen and M. Visbeck).
1011 https://doi.org/10.1029/134GM01.
1012 Knippertz, P., and Todd, M.C., 2012. Mineral dust aerosols over the Sahara: Meteorological
1013 controls on emission and transport and implications for modeling, *Rev. Geophys*., 50, RG1007,
1014 doi:10.1029/2011RG000362.

Laloyaux, P., de Boisseson, E.,Balmaseda, M., Bidlot, J.-R.,Broennimann, S., Buizza, R., et al.(2018). CERA-20C: A coupled reanalysisof the twentieth century. Journal of Advances in Modeling Earth Systems,10,1172–1195. https://doi.org/10.1029/2018MS001273.

Lamb, P. J., and R. A. Peppler, 1987. North Atlantic Oscillation: Concept and application, *Bulletin of the Amer. Met. Soc., 68*, 1218-1225.

Lau, W.K. and Kim, K.M., 2015. Robust Hadley circulation changes and increasing global dryness due to CO2 warming from CMIP5 model projections. *Proc Natl Acad Sci USA.*, 112(12):3630-5. doi: 10.1073/pnas.1418682112.

Lenssen, N., G. Schmidt, J. Hansen, M. Menne, A. Persin, R. Ruedy, and D. Zyss, 2019. Improvements in the GISTEMP uncertainty model. *J. Geophys. Res. Atmos.*, **124**, no. 12, 6307-6326, doi:10.1029/2018JD029522.

Li, J., and Ruan, C., 2018, The North Atlantic–Eurasian teleconnection in summer and its effects on Eurasian climates, *Environ. Res. Lett.* 13 (2018) 024007. DOI: https://doi.org/10.1088/1748-9326/aa9d33.

Loughe, A. F., C.-C. Lai, and D. Keyser, 1995: A technique for diagnosing three-dimensional ageostrophic circulations in baroclinic disturbances on limited-area domains. *Mon. Wea. Rev.,* **123,** 1476–1504.

Meehl G. A. and H. van Loon, 1979: The seesaw in winter temperatures between Greenland and northern Europe. Part III: Teleconnections with lower latitudes. *Mon. Wea. Rev. 107*, 1095-1106.

McHugh, M. J., and J. C. Rogers, 2001. North Atlantic Oscillation influence on precipitation variability around the Southeast African Convergence Zone, *J. Climate*, *14*, 3631- 3642.

Hersbach, H., et al., 2020: The ERA5 global reanalysis. *Quarterly Journal of the Royal Meteorological Society*, *146*(730), 1999-2049, https://doi.org/10.1002/qj.3803.

Menne, M. J., C. N. Williams, B.E. Gleason, J. J Rennie, and J. H. Lawrimore, 2018: The Global Historical Climatology Network Monthly Temperature Dataset, Version 4. J. Climate, in press. doi:10.1175/JCLI-D-18-0094.1.

Menviel, L., Govin, A., Avenas, A., et al., 2021. Drivers of the evolution and amplitude of African Humid Periods. *Commun Earth Environ* **2,** 237. https://doi.org/10.1038/s43247-021-00309-1.

Moulin, C., Lambert, C. E., Dulac, F., & Dayan, U., 1997. Control of atmospheric export of dust from North Africa by the North Atlantic Oscillation. *Nature*, 387(6634), 691.

Nie, Y., Ren, H.-L., and Scaife, A. A. 2020. Enhanced mid-to-late winter predictability of the storm track variability in North Pacific as a contrast with North Atlantic, *Environ. Res. Lett*., **15** 094037. DOI https://doi.org/10.1088/1748-9326/ab9c4d.

Nigam, S., Baxter, S., 2015. Teleconnections. In: Gerald R. North (editor-in-chief), John Pyle and Fuqing Zhang (editors). Encyclopedia of Atmospheric Sciences, 2nd edition, Vol 3, pp. 90–109. ISBN: 9780123822253.

Osborn, T.J., 2011. Winter 2009/2010 temperatures and a record-breaking North Atlantic Oscillation index. *Weather,* 66: 19-21. https://doi.org/10.1002/wea.660.

Pausata, F. S. et al., 2020. The greening of the Sahara: past changes and future implications. *One Earth* **2**, 235–250.

Pinto, J.G. and Raible, C.C., 2012. Past and recent changes in the North Atlantic oscillation. WIREs Clim Change, 3: 79-90. https://doi.org/10.1002/wcc.150.

Qin, M., Dai, A., Hua, W., 2020. Aerosol-forced multidecadal variations across all ocean basins in models and observations since 1920. Sci Adv. 6(29). doi: 10.1126/sciadv.abb0425.

Rogers, J. C., and H. van Loon, 1979. The seesaw in winter temperatures between Greenland and northern Europe. Part II: Some oceanic and atmospheric effects in middle and high latitudes. Mon. Wea. Rev., 107, 509–519.

Rohde, R. A. and Hausfather, Z., 2020. The Berkeley Earth land/ocean temperature record, *Earth Syst. Sci. Data*, 12, 3469–3479, https://doi.org/10.5194/essd-12-3469-2020.

Slivinski, L. C., and Coauthors, 2019: Towards a more reliable historical reanalysis: Improvements for version 3 of the Twentieth Century Reanalysis system. *Quart. J. Roy. Meteor. Soc.*, **145**, 2876–2908, https://doi.org/10.1002/qj.3598.

Stephenson, D., Pavan, V. & participating CMIP1 modelling groups, 2003. The North Atlantic Oscillation in coupled climate models: a CMIP1 evaluation. *Climate Dynamics* 20**,** 381–399. https://doi.org/10.1007/s00382-002-0281-5.

Thomas, N., Nigam, S., 2017. Twentieth-century climate change over Africa: Seasonal hydroclimate trends and Sahara Desert expansion**,** *J. Clim*., 31, 3349-3370, 10.1175/JCLI-D-17-0187.1

Thompson, D. W. J., Lee, S., & Baldwin, M. P., 2003. Atmospheric processes governing the northern hemisphere annular mode/north atlantic oscillation. In G. Ottersen, J. W. Hurrell, M. Visbeck, & Y. Kushnir (Eds.), *The North Atlantic Oscillation: Climatic Significance and*

Environmental Impact, 2003 (pp. 81-112). (Geophysical Monograph Series; Vol. 134). Blackwell Publishing Ltd. https://doi.org/10.1029/134GM05.

Thorne, P. W., and R. S. Vose, 2010: Reanalyses suitable for characterizing long-term trends. *Bull. Amer. Meteor. Soc.*, **91**, 353–362, https://doi.org/10.1175/2009BAMS2858.1.

van den Dool, H. M., S. Saha, and Å. Johansson, 2000. Empirical orthogonal teleconnections. *J. Climate*, **13**, 1421-1435.

van Loon, H., and J. C. Rogers, 1978. The seesaw in winter temperatures between Greenland and northern Europe. Part I: General description. *Mon. Wea. Rev*., 106, 296–310.

Visbeck, M. H.; Hurrell, J. W.; Polvani, L.; Cullen, H. M., 2001. The North Atlantic Oscillation: past, present, and future. *Proc Natl Acad Sci USA*. 2001 Nov 2001, 98 (23) 12876-12877; DOI: 10.1073/pnas.231391598.

Vizy, E. K. and Cook, K. H., 2017. Seasonality of the observed amplified Sahara warming trend and implications for Sahel rainfall, *J. Clim.*, doi: 10.1175/JCLI-D-16-0687.1.

Vose, R.S., B. Huang, X. Yin., D. Arndt, D.R. Easterling, J.H. Lawrimore, M.J. Menne, A. Sanchez-Lugo, H.-M. Zhang, 2021: Implementing full spatial coverage in NOAA's global temperature analysis. Geophysical Research Letters, 48, e2020GL090873. https://doi.org/10.1029/2020GL090873.Watanabe, M., 2004. Asian jet waveguide and a downstream extension of the North Atlantic Oscillation. *J. Clim.*, 17, 4674–4691, https://doi.org/10.1175/JCLI-3228.1.

Washington, R., James, R., Pearce, H., Pokam, W.M., Moufouma-Okia, W., 2013. Congo Basin rainfall climatology: can we believe the climate models? Phil Trans R Soc B 368:20120296.

Wei, N., Zhou, L., and Dai, Y., 2017. Observational evidence for desert amplification using multiple satellite datasets, *Scientific Reports* 7, 2043, doi:10.1038/s41598-017-02064-w.

Wohland, J., Brayshaw, D., Bloomfield, H., and Wild, M., 2020. European multidecadal solar variability badly captured in all centennial reanalyses except CERA20C, Environmental Research Letters, 15, 104 021, https://doi.org/10.1088/1748-9326/aba7e6, https://iopscience.iop.org/article/10.1088/1748-9326/aba7e6.Woollings, T., B. Hoskins, M. Blackburn and P. Berrisford, 2008. A new Rossby wave–breaking interpretation of the North Atlantic Oscillation. *J. Atmos. Sci*., 65, 609–626, https://doi.org/10.1175/2007JAS2347.1.

Wright, D.K., 2016. Humans as agents in the termination of the African humid period, *Front. Earth Sci.,* https://doi.org/10.3389/feart.2017.00004

Wu, G.X., Liu, Y., Zhu, X., Li, W., Ren, R., Duan, A., and Liang, X., 2009. Multi-scale forcing and the formation of subtropical desert and monsoon, *Ann. Geophys*., 27, 3631–3644.

Yamagata, T., Behera, S. K., Luo, J. J.,Masson, S., Jury,M. R., and Rao, S. A., 2004. Coupled Ocean-Atmosphere variability in the tropical Indian Ocean. Geophy. Monogr. 147, 189–211. doi: 10.1029/147GM12.

Zhang, Z., Ramstein, G., Schuster, M. et al., 2014. Aridification of the Sahara desert caused by Tethys Sea shrinkage during the Late Miocene. *Nature* **513**, 401–404. https://doi.org/10.1038/nature13705.

Zhou, L., Chen, H. and Dai, Y., 2015. Stronger warming amplification over drier ecoregions observed since 1979, *Environ. Res. Lett. 10*, 064012, doi:10.1088/1748-9326/10/6/064012.

Zhou, L., 2016. Desert amplification in a warming climate, *Scientific Reports* 6, 31065; doi: 10.1038/srep31065.

Zhou, L., Chen, H., Hua, W., Dai, Y., and Wei, N., 2016. Mechanisms for stronger warming over drier ecoregions observed since 1979, *Climate Dynamics*, DOI 10.1007/s00382-016-3007-9.

Zhou, L., 2021. Diurnal asymmetry of desert amplification and its possible connections to planetary boundary layer height: a case study for the Arabian Peninsula, *Climate Dynamics*, 56, 3131–3156 (2021). https://doi.org/10.1007/s00382-021-05634-x.

Zhou, L., Tian, Y., Wei, N., Ho, S-P., Li, J., 2021. Rising planetary boundary layer height over the Sahara Desert and Arabian Peninsula in a warming climate, *J. Climate*, *34*(10), 4043-4068, https://journals.ametsoc.org/view/journals/clim/34/10/JCLI-D-20-0645.1.xml.

Statements & Declarations

Funding. This work is supported by the National Science Foundation (NSF AGS-1952745 and AGS-1854486). W.H. was supported by the National Natural Science Foundation of China (42075022).

Financial interests. The authors have no relevant financial or non-financial interests to disclose.

Author Contributions. All authors contributed to the study conception and design. Data collection and analysis were performed by Liming Zhou and Wenjian Hua. The initial manuscript

was written by Liming Zhou. All authors contributed to the interpretation of results and commented on the previous versions of the manuscript. All authors read and approved the final manuscript.

Data Availability. The NCAR NAOI dataset was downloaded from https://climatedataguide.ucar.edu/climate-data/ and the NOAA NAOI dataset was downloaded from https://www.ncdc.noaa.gov/teleconnections/nao/. The NASA's GISTEMP dataset was downloaded from https://data.giss.nasa.gov/gistemp/. The BEST dataset was downloaded from https://berkeleyearth.org/data/. The ERA5 reanalysis was downloaded from https://cds.climate.copernicus.eu/#!/search?text=ERA5&type=dataset. The second Modern-Era Retrospective Analysis for Research and Applications (MERRA-2) was downloaded from https://gmao.gsfc.nasa.gov/reanalysis/MERRA-2/data_access/. The GHCNMv4 was downloaded from https://www.ncei.noaa.gov/pub/data/ghcn/v4/. The 20CRv3 was downloaded from http://apdrc.soest.hawaii.edu/datadoc/20century_reanalysisV3.php). The CERA-20C was downloaded from https://www.ecmwf.int/en/forecasts/datasets/reanalysis-datasets/cera-20c**.**